https://doi.org/10.5194/egusphere-2024-3709
Preprint. Discussion started: 13 January 2025


# Lagrangian single-column modeling of Arctic airmass transformation during HALO-$(\mathcal{AC})^3$

Michail Karalis[1], Gunilla Svensson[1,2], Manfred Wendisch[3], and Michael Tjernström[1]

[1]Stockholm University, Department of Meteorology and Bolin Centre for Climate Research, Stockholm, Sweden
[2]KTH Royal Institute of Technology, Department of Engineering Mechanics, FLOW, Stockholm, Sweden
[3]Leipziger Institut für Meteorologie (LIM), Universität Leipzig, Leipzig, Deutschland

**Correspondence:** Michail Karalis (michail.karalis@misu.su.se)

**Abstract.** In Arctic warm-air intrusions (WAIs), airmasses undergo a series of radiative, turbulent, cloud and precipitation processes, the sum of which constitutes the airmass transformation. During the Arctic airmass transformation, heat and moisture is transferred from the airmass to the Arctic environment, melting the sea-ice and potentially reinforcing feedback mechanisms responsible for the amplified Arctic warming. We tackle this complex, poorly understood phenomenon from a Lagrangian perspective, using the WAI event on 12-14 March captured by the 2022 HALO-$(\mathcal{AC})^3$ campaign. Our trajectory analysis of the event suggests that the intruding airmass can be treated as an undistorted air column, therefore justifying the use of a single-column model. In this study, we test this hypothesis using the Atmosphere-Ocean Single-Column Model (AOSCM). The rates of heat and moisture depletion vary along the advection path due to the changing surface properties and large-scale vertical motion. The ability of the Lagrangian AOSCM framework to emulate elements of the airmass transformation seen in aircraft observations, ERA5 reanalysis and operational forecast data, makes it an attractive tool for future model analysis and diagnostics development. Our findings can benefit the understanding of the timescales and driving mechanisms of Arctic airmass transformation and help determine the contribution of WAIs in Arctic Amplification.

## 1 Introduction

One of the most striking features of climate change is Arctic amplification (Serreze et al., 2000), the almost quadruple warming of the Arctic (Rantanen et al., 2022), with respect to the globe. This accentuated regional warming trend is considered to be caused by the composite effect of a multitude of local feedback mechanisms and external forcing through long-range meridional atmospheric and oceanic transport (Pithan and Mauritsen, 2014; Goosse et al., 2018; Taylor et al., 2022; Zhou et al., 2024). A substantial portion of the meridional transport occurs through episodic warm and/or most air intrusions (WAIs), driven into the Arctic by dipoles of low and high pressure systems (Woods et al., 2013; Woods and Caballero, 2016; Murto et al., 2022), typically over the Atlantic and Pacific sectors. The intruding airmasses are transformed through a sequence of physical processes, initiated upon their entrance into the Arctic. Pithan et al. (2018) offer a comprehensive summary of the typical timeline of an airmass transformation. According to their conceptual model, radiative and turbulent processes deplete the airmass' heat content (Wexler, 1936; Curry, 1983), forcing the moisture to condense into low-level mixed-phase clouds. Despite the ongoing glaciation and precipitation by the rapidly growing ice-crystals, the clouds are sustained by the continuous

https://doi.org/10.5194/egusphere-2024-3709
Preprint. Discussion started: 13 January 2025


entrainment of moisture at the cloud top, through turbulence generated by cloud-top radiative cooling (Morrison et al., 2012; Solomon et al., 2014) . As, the clouds eventually glaciate and dissipate (Taylor et al., 2022), the airmass enters a cold and dry state, which allows the characteristic surface inversion to form through surface radiative cooling, which concludes the transformation process.

Weather prediction and climate models lack the sophistication to adequately represent the complex interplay of the physical processes that drive the airmass transformation. Their main struggle lies in maintaining mixed phase clouds, with models often producing excessive precipitation, leading to the premature cloud decay and underestimation of the energy that reaches the surface through long-wave radiation (Klein et al., 2009; Morrison et al., 2012; Pithan et al., 2016). Simulating the strongly stable Arctic boundary layer and representing its coupled interaction with the sea-ice or snow covered surface is yet another challenge for current numerical models (Svensson and Karlsson, 2011; Pithan et al., 2016). There is, therefore, a dire need for establishing better understanding of the physical processes that drive airmass transformation and realistically implementing them in numerical prediction tools.

Our current understanding of Arctic airmass transformation is mainly obscured by the spatial and temporal sparsity of observations, with respect to lower latitude areas. The remote and, in some ways, hostile Arctic environment hinders the frequent deployment of lengthy in-situ scientific missions. Most of the available measurements are ship-based, collected during icebreaker expeditions (Perovich et al., 1999; Gascard et al., 2008; Tjernström et al., 2014; Cohen et al., 2017; Wendisch et al., 2019; Vüllers et al., 2021; Shupe et al., 2022) between late spring to early autumn when the sea-ice conditions allow for some flexibility in navigation. Airborn measurements from aircraft campaigns (Ehrlich et al., 2019; Mech et al., 2022) have also contributed valuable insight on the horizontal and and vertical structure of the Arctic atmosphere, but come with even greater temporal restrictions. On longer time-scales, our knowledge of the atmosphere above the Arctic Ocean is mostly based on satellite operations and reanalyses while undisrupted in-situ measurements spanning the entire seasonal cycle have only been achieved by year-long expeditions such as SHEBA (Perovich et al., 1999) and MOSAiC (Shupe et al., 2022).

Pithan et al. (2018) stress that observational and modeling activities, capable of addressing the Lagrangian aspect of airmass transformation are necessary. In lieu of such an observational framework, early attempts had resorted to trajectory analysis paired with the synthesis of observations from different stations along the approximated track (Ali and Pithan, 2020; Svensson et al., 2023). For the first time in spring 2022, however, the HALO-$(\mathcal{AC})^3$ campaign (Wendisch et al., 2024) employed a fleet of three aircrafts tracking the airmasses exchanged between the mid-latitudes and the Arctic in real time and sampling them along their advection path, offering a detailed account of the warm-air intrusion Lagrangian life cycle. The acquired datasets provide the opportunity to build process understanding, reveal the time-scales and processes that drive them and assess model performance.

Modeling the Lagrangian transformation of airmasses intruding in the Arctic has historically been attempted with the use of single-column models (SCMs, Herman and Goody, 1976; Curry, 1983; Cronin and Tziperman, 2015; Pithan et al., 2016; Fitch, 2022) and Large Eddy Simulating (LES) tools (Dimitrelos et al., 2023). All studies, to date, have adopted idealized frameworks, bypassing the complexity of imporant drivers of the airmass transformation, such as the sea-ice atmosphere interaction (e.g. using fixed values for temperature and other sea-ice and snow properties) and/or the dynamical forcing such as advection and

https://doi.org/10.5194/egusphere-2024-3709
Preprint. Discussion started: 13 January 2025


large-scale subsidence. However, thorough understanding of the processes and timescales of airmass transformation can not be achieved solely through idealized experiments. For that purpose, simulating real cases and comparing with observations is necessary (Pithan et al., 2016), but emulating the advection and Lagrangian transformation of WAIs with the mere use of a column model seems, at first glance, complicated. However, Svensson et al. (2023), through trajectory analysis of the two WAIs captured by MOSAiC in April 2020, showed that air parcels across the lower troposphere aligned vertically for approximately two days before reaching the central Arctic, resembling an undistorted atmospheric column. To the extent that such a flow pattern is generally representative of WAIs, it suggests that the intruding airmasses maintain a column-like structure during their poleward advection, therefore facilitating the use of SCMs for their simulation.

In this study, we extend the trajectory methodology in Svensson et al. (2023) on the WAI captured by HALO-$(\mathcal{AC})^3$ on March 12, 2022 and find a similar column-like flow pattern. The suite of Lagrangian observations available for this case makes it a suitable testbed for the development of a Lagrangian single-column modeling framework to study real WAI cases, as per Pithan et al. (2016, 2018)'s suggestions, using the Atmosphere-Ocean Single-Column Model (AOSCM, Hartung et al., 2018). We use the model to investigate the processes that drive the airmass transformation. We compare our simulations to observations, ERA5 and IFS forecast data in order to assess the performance of the model and its potential as a tool to test and construct future model parameterizaton schemes.

## 2 Data and Methods

### 2.1 Observations

The HALO-$(\mathcal{AC})^3$ campaign (Wendisch et al., 2024) was launched in March 2022 aiming to observe the transformation of the airmasses exchanged between mid-latitude regions and the Arctic from a quasi-Lagrangian perspective. The first warm-air intrusion episode occurred at the start of the campaign. A warm and moist airmass was steered into the Arctic between a low pressure system, traveling poleward along the east coast of Greenland, and a high-pressure system over Europe. Using forecast data and trajectory analysis in preparation of the flight tracks (Fig. 1), the High Altitude and LOng-range (HALO) research aircraft followed the airmass for three days (March 12th to 14th) into the Arctic, sampling it daily. During consecutive research flights RF02, RF03 and RF04 (Wendisch et al., 2024), a total of 50 dropsondes were released along the axis of the advection over the Fram Strait, covering a distance of approximately 10 latitudinal degrees (71°N-81°N).

We use the dropsonde-derived vertical profiles of temperature, specific humidity and horizontal wind, from approximately 12 km to the surface, to illustrate the observed Lagrangian evolution of the airmass and evaluate its representation in the model.

### 2.2 Lagrangian trajectories

In order to approximate the advection path of the airmass, we use LAGRANTO (Sprenger and Wernli, 2015), a Lagrangian trajectory calculation and analysis tool, here applied on the three-dimensional ERA5 (Hersbach et al., 2020) wind field. ERA5 can be considered a reliable representation of the atmosphere (Graham et al., 2019) due to its global coverage, relatively high

https://doi.org/10.5194/egusphere-2024-3709
Preprint. Discussion started: 13 January 2025


spatial and temporal resolution (here $0.25° \times 0.25°$ on the horizontal plane and 137 vertical levels on an hourly timestep) and, lastly, the continuous assimilation of in situ and satellite observations within 12-hour windows.

On March 13, at 12 UTC we launch 24-hour long trajectories, 600 in total, half of which were computed backward and half forward in time. All trajectories are initialized within a 100 km radius from the center of the sampled area (81°N, 5°E, see Fig. 2a) at pressure levels 500, 600, 700, 800, 850 and 900 hPa (Fig. 2b). Their initialization at this location serves a dual purpose: i) the use of more realistic ERA5 wind fields in this region at the time of initialization due to the abundance of dropsonde profiles available for assimilation (Hersbach et al., 2020), and ii) more matches between trajectory and observational points which enables the comparison. We assessed the stationarity of the synoptic flow by computing additional trajectories within a 2-hourly window around the selected initialization time, which showed negligible changes. We test whether the trajectories adhere to the same vertical alignment pattern suggested by Svensson et al. (2023), by searching for trajectories at different pressure levels that maintain the smallest relative distances (Fig. 2b). We consider this trajectory ensemble to be indicative of the airmass path and use it to simulate the Lagrangian airmass transformation.

### 2.3 Airmass detection

We provide an estimate of the WAI's spatial extent by following along the trajectory ensemble ( Sect. 2.2) and, at each timestep, scanning the neighboring ERA5 grid cells in the direction perpendicular to the mean flow to locate the edges of the advected airmass. These are identified using an integrated vapor transport (IVT) threshold of 100 kg $m^{-1}$ $s^{-1}$, generally preferred for Arctic WAI and AR detection (Gorodetskaya et al., 2014; Guan and Waliser, 2015; Woods et al., 2013). IVT values during the March 12-14, 2022 WAI event lie roughly between 120 and 220 kg $m^{-1}$ $s^{-1}$ (Walbröl et al., 2024), making the 100 kg $m^{-1}$ $s^{-1}$ appropriate for the airmass detection. We compute the total IVT as the vector sum of the meridional and zonal components, derived from ERA5, to account for potential changes in the direction of transport from mainly meridional to zonal as the airmass crosses the Arctic (Fig. 2b,c).

Information on the extent of the airmass is necessary for determining its internal spatiotemporal variability and understanding the different transformation pathways that can be encountered within it. Within the margins of the moist plume, we look for profiles of temperature, humidity, wind speed and cloud liquid and ice water content of similar structure to the profiles on the trajectories. Correlation is examined only within the lowest 3 km, where variability is expected to be larger, and is assessed using the Pearson correlation coefficient. The correlation range ($P_{co} > 0.5$) marks the extent of what could be considered a column-like airmass that is uniformly transformed along the trajectory ensemble (Fig. 2c). In contrast, the parts of the plume that fall outside the correlation range are airmasses whose evolution can not be represented by the selected trajectory ensemble.

### 2.4 Model description and Lagrangian simulations

The Atmosphere-Ocean Single Column Model (AOSCM, Hartung et al., 2018) follows the development version of EC-Earth (Döscher et al., 2022), in an 1D framework. In the AOSCM, the SCM version of the atmospheric model OpenIFS cy43r3 (Open Integrated Forecasting System; https: //confluence.ecmwf.int/display/OIFS/About+OpenIFS, last access: 26 November 2024) is coupled to a column of the ocean model NEMO3.6 (Nucleus for European Modelling of the Ocean; https://www.

https://doi.org/10.5194/egusphere-2024-3709
Preprint. Discussion started: 13 January 2025


nemo-ocean.eu/, last access: 26 November 2024) through the OASIS3-MCT coupler (https://oasis.cerfacs.fr, last access: 26 November 2024). Sea-ice processes in NEMO are here represented by LIM3 (Rousset et al., 2015) . In an Eulerian framework, information of the large-scale flow is easily introduced into the model through the prescribed forcing. The model uses ERA5 vertical velocity profiles ($\omega$) to include the effect of large-scale divergence, geostrophic wind profiles for the application of a pressure gradient forcing on the column while advection of heat, moisture, cloud water and momentum is represented with the introduction of an advective tendency term in the state variables' prognostic equations. A detailed guide for designing and executing AOSCM experiments is given in Hartung et al. (2018, 2022).

In order to follow the Lagrangian evolution of the airmass with the AOSCM, we set the advective tendencies to zero, inhibiting the inflow(outflow) of heat, moisture or momentum from(to) the ambient atmosphere. The atmospheric column is made aware of its poleward advection through the temporally varying surface conditions and large-scale dynamical forcing, the details of which (surface type, surface temperature and large-scale subsidence) along the predesignated airmass tracks obtained from ERA5 reanalysis data (Sect. 2.2). Pressure-gradient forcing leads to the emergence of inertial oscillations close to the surface, which lead to unphysical surface fluxes of heat and momentum. In order to suppress these spurious oscillations we nudge the horizontal wind to the ERA5 profiles throughout the entire column and set the nudging timescale ($\tau_{nudge}$) to be equal to the model timestep (15 min).

The sharp changes in surface properties require the division of each trajectory into three legs: ocean, marginal ice zone and sea-ice. The airmass spends approximately 21, 6 and 22 h over each leg, traveling 1500, 340 and 1025 km distances respectively. Over ocean, the inclusion of the sea-surface temperature (SST) meridional gradient is crucial, whereas the two-way sea-atmosphere interaction is less relevant, considering the high speed of advection. The standalone atmospheric model is therefore more well-suited for this part of the simulation since it allows for the prescription of the SST evolution, for this part of the simulation.

As the airmass flows over the marginal ice zone (MIZ, sea-ice fraction $> 0.15$ and $< 0.9$), the crude treatment of sea-ice in OpenIFS becomes increasingly problematic, making the coupled configuration more suitable. In coupled mode, the AOSCM allows for a more realistic representation of the sea-ice thickness and grid-scale variability. The presence of snow on ice, not allowed in OpenIFS, has also been shown to mitigate surface energy and near-surface air-temperature biases (Pithan et al., 2016). The start of the third and final leg, is marked by the sea-ice fraction increase above 0.9. The sea-ice model for both legs is initialized using ERA5 information for the sea-ice area concentration. ERA5 is also used for the initialization of sea-ice temperature, although an adjustment is necessary for the model to be able to produce realistic skin temperature values, comparable to the respective mean ERA5 values for each leg. The thickness of the sea-ice and snow layers as well as profiles of the oceanic temperature, salinity and currents are obtained from the CMEMS Global Ocean Physics reanalysis dataset (https://doi.org/10.48670/moi-00016).

At each transition point between surface regimes, the modeled profiles at the final timestep of the previous simulation are used as initial conditions for the following simulation. Over each sea-ice leg, two additional preparatory simulations are performed; the first one using the standalone OpenIFS model to produce a first estimate of the surface energy fluxes needed for the ice-model at the first time-step, and the second one using the coupled model for a 2-hour long simulation, in order to reach

https://doi.org/10.5194/egusphere-2024-3709
Preprint. Discussion started: 13 January 2025


a sea-ice state that is more in balance with the atmosphere. This helps mitigate abrupt spikes in the surface energy fluxes at the beginning of the third simulation leg.

## 3 Results and Discussion

### 3.1 Large-scale setting and airmass transport

On 12 March, 2022, a low-pressure system develops over the south-east coast of Greenland and a strong high-pressure system extended over Scandinavia (Walbröl et al., 2024), creating a meridional path for the warm and moist mid-latitude air to enter the Arctic (Fig.1a). From a climatological perspective, this dipole flow configuration over the North Atlantic is the most common driver of Arctic moist intrusions, responsible for about 75% of the events (Papritz et al., 2022). Despite the Greenland low weakening, meridional advection persists through March 13 (Fig.1b), sustained by the development of a new low, west of the United Kingdom. On March 14 (Fig.1c), the south Greenland low deepens once again, due to the arrival of strong cyclone from the southwest, and connects with a smaller cyclone forming over north Greenland. This configuration causes the isobars to curve and displaces the flow to the east as the airmass approaches the North Pole. This extensive low-pressure system stretching over Greenland, in combination with the persistent Scandinavian blocking, sets up for yet another WAI into the Arctic in the following days (Walbröl et al., 2024).

Trajectories initialized over the MIZ at different pressure levels within the advection layer show the path of the airmass (Fig. 2a). The moist airmass flows over the Atlantic, along the 0° meridian for 24 hours, reaching the MIZ at around 10 UTC on March 13 and the central Arctic around 24 hours later. The trajectories slowly spread out on both ends, with their maximum in-between distance ranging from 200 km over the MIZ (the diameter of the circle within which they were initialized) to around 700 km (Fig. 2a). Within this large suite of trajectories, smaller subsets can be found, comprised of one trajectory per pressure level, that exhibit a considerably narrower spread, to the point where they appear roughly vertically aligned. The subset closest to observations is pictured in Fig. 2b, with maximum width around 260 km.

Vertical alignment within parcels traveling at different heights suggests that the airmass maintains a consistent column-like structure throughout its 49-hour journey into the Arctic. We examine whether the advection and transformation of the airmasses around the trajectories is similar enough for them to be likened to a cohesive atmospheric column. The trajectory ensemble runs through the narrow center of the meridional transport corridor where IVT values are the highest (around 350 kg $m^{-1}$ $s^{-1}$ in the southernmost end to approximately 150 kg $m^{-1}$ $s^{-1}$ near the North Pole, Fig. 2c). The correlation range (hatched section), which envelops columns of similar vertical structure (see Sect. 2.3) becomes thinner with time but consistently encompasses the entire trajectory ensemble. Therefore, all trajectories within the ensemble can be regarded as representative of the same air column.

Vertical alignment in Arctic WAIs has also been encountered in past studies (Ali and Pithan, 2020; Svensson et al., 2023). To the degree that this feature is common among WAIs, it facilitates the exploration of Arctic airmass transformations with simple 1D models such as the AOSCM. The framework can be applied on more WAI case studies, while the results can be used to evaluate and build on our theoretical understanding of such events (Pithan et al., 2018).

https://doi.org/10.5194/egusphere-2024-3709
Preprint. Discussion started: 13 January 2025


### 3.2 Spatial variability of airmass transformation in ERA5

The along-stream transformation of the airmass is shown in Fig. 3 in terms of integrated column water (vapor, liquid and ice) (Fig. 3a-c) and surface energy budget (SEB) terms (Fig. 3d-i). The integrated water vapor (IWV) content of the airmass is initially rather high, 16 kg m$^{-2}$ on average (Fig. 3a) and decreases as the airmass advances northward, slowly over the ocean but more rapidly over ice, to about half of the initial value. The majority of the moisture is gathered towards the center of the airmass (0° longitude over the ocean where the spatial gradient is more evident) and dropping towards the edges, while the spatial extent of the airmass also varies along the advection path. The western sector of the airmass is more susceptible to the synoptic systems developing over Greenland (Fig. 1), which explains the occasional westward divergence of the moisture (e.g. westward spread towards the Greenland coast at around 70°N, as well as later on, north of Svalbard).

Measurements conducted within 250 km and 3 h of a trajectory point are considered suitable for comparison (11 out of 50 dropsondes). The dropsonde profiles included in the correlation range are in general agreement with the ERA5 IWV content, although appearing slightly drier over the ocean and moister over the MIZ (Fig. 3a). The profiles located on the eastern boundary of the airmass show a consistent mismatch with ERA5 data, in most cases, severely lacking in moisture content. It is likely that observations at these locations are capturing the steep moisture gradient at the airmass boundary, unable to be represented in ERA5 either due to i) ERA5's resolution or ii) the quality controls built in the assimilation scheme potentially filtering the profiles out triggered by large deviations between the observations and the forecasted values (Hersbach et al., 2020).

The spatial variability is even more prominent in the cloud liquid water path (LWP, Fig. 3b) fields, with most of the cloud liquid water found west of the prime meridian for the time the airmass spends over the ocean. The LWP is abruptly depleted as the air mass crosses the MIZ and remains small all the way into the central Arctic. The depletion of the liquid cloud over the MIZ is concurrent with an increase in the ice water path (IWP, Fig. 3c). The glaciation of the cloud is visibly accelerated at higher latitudes, near the northernmost end of the trajectories.

The spatial distribution of the cloud water within the airmass is also reflected in the net shortwave radiation flux at the surface (Fig. 3d) during daytime. On the western flank of the airmass, where the LWP is larger, less solar radiation reaches the surface but the down-welling long-wave radiation emitted by the liquid clouds changes the sign ofthe net surface long-wave flux to positive (Fig. 3e). In the eastern sector, the weaker cloud presence is not able to compensate the upwelling longwave radiation emitted by the warmer surface (Fig. 3f), yielding a negative radiative balance (Fig. 3e). Once the airmass flows over sea-ice, the long-wave radiation becomes a consistent net source of energy for the surface.

Despite the large meridional skin temperature gradient − more than 20 °C (Fig. 3f) between southernmost to northermost end of the trajectory ensemble − the airmass is consistently warmer than the surface, losing energy to it through the turbulent sensible heat flux throughout its Arctic journey (Fig. 3g). The spatial variability in skin temperature over the ocean also appears to be controlling the exchange of latent heat at the surface (Fig. 3h). Over the warm ocean, the strongly negative (upward) fluxes indicate the ongoing moisture uptake by the airmass. Over colder waters, the latent heat fluxes turn positive (downward) and

https://doi.org/10.5194/egusphere-2024-3709
Preprint. Discussion started: 13 January 2025


are of similar magnitude as over the sea ice covered surface, implying a persistent water vapor deposition from the airmass onto the oceanic surface.

The sum of the all radiative and turbulent surface fluxes yields the surface energy budget (SEB) depicted in Fig. 3i. Along the trajectories, the surface receives the most energy within the first few hours, largely due to the contribution of the solar radiation. However, in the absence of sunlight, the SEB shows a strong zonal gradient over the ocean. Two distinct regimes can be identified. In the positive SEB regime (western sector of the airmass), energy is transferred from the airmass to the surface ($\sim$ 50 W m$^{-2}$) through both longwave radiation and turbulent heat exchange. In the negative SEB regime ($\sim$ -50 W m$^{-2}$) on the eastern side, the ocean temperatures are high and the liquid cloud cover is low, causing the upward latent heat and long-wave radiation to outweigh the down-welling sensible heat flux. Our trajectory ensemble runs between the two regimes, favoring the negative regime for the first 10-12 hours and crossing through to the positive regime from then onwards. Entering the MIZ, the SEB becomes uniformly positive across the airmass. Most of the energy received by the surface ($\sim$ 60 W m$^{-2}$) is contributed by turbulent heat fluxes. Farther into the Arctic, the SEB reaches 75 W m$^{-2}$, with mainly the sensible heat flux and, to a lesser degree, the latent heat and the downward emitted long-wave radiation counteracting the surface radiative cooling. The timeline of the SEB during the intrusion shows the strong impact on the Arctic system, as well as the effect of the surface forcing on the airmass transformation.

### 3.3 Modeling the airmass transformation

We have established that the vertical alignment of the trajectories within the advection layer gives merit to the simplified view of the intruding airmass as an atmospheric column. However, despite the spatial and temporal proximity within our trajectory ensemble, the initial profiles and alongstream forcing (surface and horizontal/vertical wind conditions) of each individual member show slight differences. In order to represent this variability, which we argue to be representative of the airmass variability (see Sect. 3.2), we use the entire trajectory subset (6 trajectories) to perform ensemble simulations. This approach gives some insight on both the mean characteristics of the airmass transformation, but also reveal its sensitivity to each of the participating forcing factors. We use all initial profiles paired with their respective alongstream surface and subsidence conditions.

We consider the airmass transformation to be taking place within a 5 km deep layer above the surface. This consideration stems from i) the initial rich moisture content of this layer comprising approximately 96% of the total moisture content of the column and ii) the vertical alignment feature among trajectories at pressure-levels between 900 hPa (approximately 0.8 to 1 km on average) and 500 hPa (around 5 km) that motivated our single-column model framework. We do not include trajectories within the boundary layer in our ensemble, due to the expectation that the friction-induced wind shear and veer (vertical gradients in wind speed and direction respectively) near the surface would cause air-parcels to move in different directions to the rest of the airmass. However, we also expect the interaction with the changing surface properties through vertical mixing to be driving changes in the boundary layer properties more strongly than any potential differential advection, leading us to treat the boundary layer as part of the advected air-column.

https://doi.org/10.5194/egusphere-2024-3709
Preprint. Discussion started: 13 January 2025


We use the mean temperature of the lowest 5 km ($\overline{T}_{5km}$) and the vertically integrated water vapor content over the same layer (IWV$_{5km}$) as indices for the heat and moisture content of the airmass respectively. Their relative evolution (Fig. 4) enables identification of potential heat and moisture sources/sinks and their effective timescales on the airmass transformation along the trajectories. Along with the AOSCM simulations we also present ERA5 and IFS Cy47r3 operational forecast data (IFS-OF) in order to test the consistency in the results between the Lagrangian and Eulerian modeling approaches. Finally, the dropsonde observations collected along the airmass path are synthesized to demonstrate the observed Lagrangian evolution of the airmass' heat and moisture.

#### 3.3.1 Transformation over the ocean

The initial state of the airmass is depicted in the top right corner of Fig. 4. Since the AOSCM is initialized with ERA5 data, the initial state between the two products is identical (13.3 kg m$^{-2}$ and -2.2 °C). IFS-OF shows a slightly moister airmass (by 0.5 kg m$^{-2}$). The curves display a steep slope during the advection over ocean, more prominent in ERA5 and AOSCM, indicating a faster loss of heat over moisture. The total cloud water content of the airmass, liquid in its majority, evolves similarly to the moisture. The overall changes sum up to 2.5 °C for temperature and a mere 0.5 kg m$^{-2}$ for moisture, on average, for the AOSCM and ERA5. For IFS-OF the respective changes are 2.3 °C and and 1 kg m$^{-2}$ .

The standard deviation is shown with faded lines perpendicular to the main curves and depicts the variability. At the southernmost point of the airmass, all products agree on a standard deviation of approximately 0.7 kg m$^{-2}$ for IWV and 0.1 °C for temperature. The variability around the curves drops for ERA5 and IFS-OF, due to the trajectories converging when approaching the MIZ, while for the AOSCM it expands, showing an increase of 0.5 kg m$^{-2}$ and 0.5 °C for moisture and temperature respectively. The slight tilt in the faded perpendicular lines shows the uncertainty in the predicted airmass heat content growing with simulation time. Observations over the ocean (black dots) show a large scatter, especially in IWV$_{5km}$. The AOSCM uncertainty range is wide enough to encompass the observed variability. It should be noted that the observational data points presented in Fig. 4 do not include the dropsondes released close to the edge of the moist airmass (71°N, 4°E and 78°N, 7°E in Fig. 3a) and are, expectedly, not representative of its evolution.

#### 3.3.2 Transformation over the MIZ

Over the MIZ (denoted with dashed lines in Fig. 4), there is a distinct change in the evolution of the airmass showcased by all considered products. The slope of the curves becomes flatter, pointing to the more rapid loss of moisture and a comparatively slower decrease in the heat content. The AOSCM shows a 1 kg m$^{-2}$ decrease in IWV$_{5km}$ and a 0.6 °C cooling, while the standard deviation remains mostly unchanged. In ERA5, the $\overline{T}_{5km}$~IWV$_{5km}$ slope momentarily reverses, suggesting a short-lived heating of the 5 km layer upon the airmass entrance in the MIZ. This abrupt change is coincident with the start of a new ERA5 assimilation window (at 9 UTC) and is, most probably, related to the adjustment of the airmass state to the numerous available dropsonde observations available over MIZ at that time. By the end of the MIZ leg, ERA5 heat and moisture drops to values comparable to the ones predicted by the AOSCM. The IFS-OF shows a less severe change in slope, with the moisture and temperature content changes of the same order as over the ocean. However, it is important to note that the residence time of the airmass over ocean and MIZ is substantially larger. In that context, the weakening of the airmass cooling is more modest while the acceleration of the moisture depletion is striking. Observations over the MIZ show a similar $\overline{T}_{5km}$~IWV$_{5km}$ trend, agreeing with the timescales of heat and moisture loss, but displaying higher absolute IWV values as big as 1 kg m$^{-2}$ compared to AOSCM and ERA5. The IFS-OF curve is, interestingly, in closer agreement with the observed values.

### 3.3.3 Transformation over sea-ice

The most drastic part of the transformation takes place over sea-ice. For the AOSCM, the slope of the curve becomes steeper, indicating the loss of both heat and moisture at a much faster rate. Cooling is stronger in the first half of the sea-ice leg and slows down again towards the end, with moisture loss being more dominant. At the same time, the total cloud water content grows and gradually converts from liquid to ice by the end of the simulation. The ERA5 appears to be lagging behind in moisture loss at the beginning of the sea-ice leg, compared to the AOSCM simulations, but agrees on the final state of heat and moisture content, as well as cloud phase. IFS-OF shows the opposite trend; excessive drying during the first half and enhanced cooling during the second, still in the end predicting an airmass state of similar moisture content but colder by 1 °C while still maintaining liquid clouds. The uncertainty range ERA5 and IFS-OF curves grows larger due to the slight divergence of the trajectory ensemble. In contrast, the uncertainty range for the AOSCM appears to be narrowing down again to its initial value (0.7 kg m$^{-2}$) for IWV$_{5km}$ but it is and order of magnitude larger for $\overline{T}_{5km}$ compared to the initial state (almost 1 °C), which is a range comparable to IFS-OF.

AOSCM, ERA5, IFS-OF and observations all show a similar heat-to-moisture content evolution. Similarities between ERA5 and AOSCM are less surprising since ERA5 data was used for initialization and forcing of the AOSCM. However, the AOSCM is also able to reproduce an airmass transformation of magnitude and timescales comparable to its 3D counterpart, IFS-OF. The observed airmass transformation, to some extent, displays similar features. However, comparison is hindered by the large scatter of observations and their confinement within a small area around the MIZ. Several factors could be contributing to this scatter. These include i) the spatial inhomogeneity of the airmass properties that is not entirely represented by our small trajectory ensemble, ii) the relative horizontal displacement of the dropsondes during their descent (some of them could be landing closer to or in the MIZ) and, iii) in some cases, the time intervals between measurements in the same area being large enough to allow changes related to advection.

In terms of model uncertainty, the initial ensemble spread in the airmass properties is almost solely attributed to the differences in initial moisture content. At the end of the simulation, due to slight variations in the forcing among the trajectory ensemble, uncertainty in the heat content grows as well. The same behavior is exhibited by the airmass in ERA5 and IFS-OF, with the latter even matching the simulated magnitude of the spread. The AOSCM, if appropriately forced, is, therefore, able to represent the physical processes that drive the airmass transformation.

https://doi.org/10.5194/egusphere-2024-3709
Preprint. Discussion started: 13 January 2025


#### 3.3.4 Vertical structure

The transformative physical processes often act in different layers within the atmosphere. Therefore, in addition to the bulk changes in the mean or integrated airmass properties, changes in the vertical structure of the airmass also need to be considered in order to draw a comprehensive picture of the airmass transformation.

Our initial airmass appears to be warm and moist with the boundary layer reaching a depth of just over 1 km on average (Fig. 5a). The boundary layer is diagnosed in the model as the layer adjacent to the surface within which the Bulk Richardson number is below the critical the threshold ($Ri_c$ = 0.25). The ensemble variability in the boundary layer depth estimate is overall small ( $\sim$ 30 m) except for the first 8 h of the simulation when it reaches up to 100 m. The boundary layer remains stably stratified throughout the simulation (Fig. 5d), with the air within the boundary layer constantly losing heat to the surface. The near-surface cooling intensifies as the airmass flows over the MIZ with a surface inversion starting to develop and the boundary layer becoming shallower. As the airmass moves past the MIZ and over fuller sea-ice cover, the cooling extends through a deeper column within the atmosphere. Cooling aloft (1 - 5 km) weakens the surface inversion and leads to a slight boundary layer deepening by the end of the simulation. The uncertainty of the predicted thermodynamic structure, in terms of ensemble standard deviation, grows with simulation time. The largest values are encountered over sea-ice between 1 and 4 km of altitude and are seemingly related to ensemble variability in the simulated cloud height and overall presence.

Most of the moisture is contained in the lowest 2 km (Fig. 5g), suggesting a recent uptake over the North Atlantic, a common source region of moist intrusions according to Papritz et al. (2022). Despite the constant decline in the near surface temperature through turbulent processes, the airmass takes up moisture from the surface during the first 12 h of the simulation. From around 12 h and onwards, while still over the ocean, the latent heat fluxes turn negative and the boundary layer is slowly depleted of its moisture while the drying is accelerated as the airmass enters the MIZ and progresses farther into the Arctic.

The cloud in the AOSCM simulations initially consists of a single, solely liquid cloud layer at 1 km over the ocean surface, right on top of the boundary layer which remains stable throughout the simulation (Fig. 5j). The cloud deck splits into two layers at around $t = 12$ h and later, over the MIZ, a third liquid cloud layer is formed within the boundary layer. Finally, moving over higher sea-ice concentrations, the cloud starts rising from the surface (Fig. 5j). The first signs of cloud glaciation appear as a response to cloud-top radiative cooling while ice clouds emerging at higher altitudes at the end of the ocean leg (Fig. 5m). Later on, the cloud specific ice content increases at the expense of the cloud liquid, due to the upward rise of the cloud and the accompanied adiabatic cooling (Fig. 5s).

The wind is initially strong, exceeding 25 m s$^{-1}$ at higher altitudes but also near the top of the boundary layer in what appears to be a low-level jet (Fig. 5p). The airmass gradually loses momentum throughout the column. When it reaches the MIZ, the additional surface-induced friction causes an additional deceleration on the wind within the PBL. Later in the simulation, over higher sea-ice concentrations, the near-surface wind-speed increases again, in a jet-like structure around 0.5 km, while the wind in the overlying layers slows down.

In terms of the vertical wind, $\omega$ (Fig. 5s) is weak over the ocean, with the sign often alternating over the height of around 2 km. The vertical wind divergence within the liquid cloud is partially causing the cloud-layer to split (Fig. 5j). Over the MIZ, the

https://doi.org/10.5194/egusphere-2024-3709
Preprint. Discussion started: 13 January 2025


subsidence spikes abruptly and over the sea-ice leg the vertical motion is predominantly upward, with $\omega$ increasing the deeper the airmass intrudes into the Arctic. The strong large-scale updraught in the AOSCM simulations and ERA5 data (Fig. 5s-t) coincides with the the cloud water phase transition from liquid to ice (Fig. 5j-k and m-n at t $\simeq$ 27 h) which is due to the induced adiabatic cooling. The ensemble $\omega$ standard deviation is also rather large, within the range of [0.05, 0.25] Pa s$^{-1}$, almost as large as the signal itself. Deviations of that magnitude have been shown to have a considerable impact on the evolution of the cloud layer (Mirocha and Kosović, 2010; Neggers, 2015; Young et al., 2018; van Der Linden et al., 2019).

ERA5 and the IFS-OF (Fig. 5 middle and right columns) show a similar airmass transformation time-line with that simulated by AOSCM. The strengthening of the boundary layer stability is slightly delayed in ERA5 and the IFS-OF (Fig. 5e-f), presumably because of difference in the treatment of snow/sea-ice and atmosphere coupling between AOSCM and the two 3D products. OpenIFS, the model responsible for the production of both IFS-OF and -in part- ERA5 data, uses a sea-ice layer of fixed thickness (1.5 m), entirely disregarding the presence of snow on top of sea-ice, while the AOSCM is only set up to reproduce the bulk changes in the sea-ice surface temperature (see Sect. 2.4), therefore potentially misrepresenting their timing. By the end of the trajectories, however, the ERA5 and IFS-OF inversion grows stronger than what the AOSCM is able to simulate, resulting to a shallower boundary layer in comparison. Additionally, the boundary layer over the ocean is drier in ERA5 and IFS-OF (Fig. 5h-i); the near-surface specific humidity remains constant for the first 8 h of the transformation before dropping. The ensemble standard deviation for all ERA5 and IFS-OF variables is maximum at the start and the end of the transformation, decreasing over the MIZ, at around 24 h, when the trajectories converge and therefore cross fewer grid points.

The ERA5 (Fig. 5h) cloud structure matches the AOSCM's, more so over the ocean than over the sea-ice, showing a similar split of the cloud layer over the MIZ and comparable time-scales for the cloud-water phase transition (Fig. 5k-n). The cloud in IFS-OF (Fig. 5i) bares smaller resemblance to AOSCM than to ERA5, especially over the ocean where the cloud exhibits discontinuities and smaller liquid water content and over sea-ice where the IFS-OF specific ice content is notably smaller (Fig. 5l-o). However, the multi-layer liquid cloud structure over the MIZ and early sea-ice leg is found in all three products.

The use of ERA5 data for forcing the AOSCM is partly the reason behind the stark similarities between the two products. The strong wind nudging ($\tau$ = 900 s) and prescribed vertical velocities ($\omega$), explaining the identical appearance of Fig.5p,q and Fig.5s,t respectively, are influencing the changes in the thermodynamic and cloud structure of the airmass. The larger differences between IFS-OF and AOSCM are, therefore, to be expected, especially when considering that the trajectories, along which we study the airmass transformation, were computed on ERA5 data. This is evident in the stronger IFS-OF baroclinic wind-shear over the ocean and MIZ compared to ERA5 (Fig. 5q-r) which could lead to a different airmass path and a smaller degree of vertical alignment between the trajectories. The vertical velocity $\omega$ is also different in IFS-OF, exhibiting larger temporal and spatial variability both in the mean signal as well as the ensemble standard deviation (Fig. 5u).

#### 3.3.5 Comparison with observed transformation

We synthesize the dropsonde profiles of temperature and moisture taken along the airmass path to evaluate whether the modeled and observed observed airmass transformation exhibit the same features and timescales (Fig. 6). The majority of observations suitable for comparison are gathered around the MIZ area (Fig. 2). To make the comparison more convenient, we cluster the

https://doi.org/10.5194/egusphere-2024-3709
Preprint. Discussion started: 13 January 2025


measured profiles according to the surface type they are conducted over: ocean (Fig. 6a-e), MIZ (Fig. 6f-j) and sea-ice (Fig. 6k-o). For the clustering we use the ERA5 sea-ice concentration of the nearest grid at the time closest to the dropsonde launch. The ensemble mean AOSCM, ERA5 and IFS-OF profiles in the center of each dropsonde cluster. Over the ocean, observations show a temperature profile similar to AOSCM, ERA5 and the IFS-OF, with the exception of a layer between 2 and 4 km that appears to be generally cooler in the dropsonde measurements (Fig. 6a). The observed air temperature near the surface is slightly positive, approaching zero, which is consistent with ERA5 and IFS-OF. In contrast, AOSCM simulates a drop in temperature below freezing levels. Dropsondes released over full sea-ice cover, show minor surface cooling but an otherwise unchanged temperature and structure. The AOSCM seems to be more responsive to the advection over the sea-ice, showing a more dramatic reduction of temperature near the surface compared to the observations, ERA5 and IFS-OF (Fig. 6k,l).

Variability in the observed specific humidity profiles is significant, especially over ocean (Fig. 6b). Two of the dropsondes match the AOSCM profile closely, while the third is considerably drier than all products. ERA5 and IFS-OF show a similar magnitude of specific humidity to the AOSCM except in the lowest 1 km where they both show a consistent deficit of approximately 0.3 g $\mathrm{kg}^{-1}$. The airmass is observed to get progressively drier as it is advected over sea-ice (Fig. 6g,l). Similarly to the cooling rate, the drying rate near the surface is overestimated by the AOSCM (Fig. 6l)

The airmass stratification remains strong over all surface types as demonstrated by the virtual potential temperature profiles, $\theta_v$ (Fig. 6c,f,g). Observations over ocean and, more so, the MIZ show small inversions within the first 2 km (Fig. 6f,g). These inversions possibly correspond to a multi-layer cloud structure that agrees with our AOSCM simulations, as well as ERA5 and IFS-OF (Fig. 6j).

The strong nudging in our AOSCM simulations makes the horizontal wind identical to ERA5 and, thus, comparable in magnitude and structure to observations (Fig. 6d,i,n). The largest differences are noted, once again, in the lowest 2 km over the MIZ, where measurements capture a considerably stronger jet than the one in ERA5 and IFS-OF (Fig. 6i).

#### 3.3.6 Physical and dynamical drivers

In order to reveal the physical mechanisms responsible for the different stages of the transformation we break down the changes in temperature and moisture (Fig. 7) within the airmass into the individual contributions of the participating physical parameterization schemes. These mechanisms impact different layers within the airmass: the planetary boundary layer (PBL), the cloud layer and the air aloft. We use the $\mathrm{Ri}_{bulk}$ based diagnostic to isolate the PBL (see Sect. 3.3.4). The cloud layer is identified as the layer between the PBL top and the liquid cloud layer top, therefore not including PBL clouds and ice clouds at altitudes higher than the liquid layer. Clouds exclusively in the ice phase are therefore shown in the residual layer between the cloud layer top and 10 km. In Fig. 7 we show the ensemble mean physical tendency profiles contributed by each parameterization scheme, over the three different legs of the trajectories (ocean, MIZ, ice), for each of the three layers defined above (PBL, cloud, 10km) separately, normalized by their individual depths.

In the AOSCM, long-wave radiative cooling is a prominent heat sink for the airmass throughout intrusion (Fig. 7a). Radiative cooling near the surface is largest over the ocean, approximately $-0.2$ K $\mathrm{h}^{-1}$, where the near-surface air is warmest and moistest and drops to $-0.1$ K $\mathrm{h}^{-1}$ over the MIZ and sea-ice. The ensemble median cooling rates derived from the radiation scheme

https://doi.org/10.5194/egusphere-2024-3709
Preprint. Discussion started: 13 January 2025


also spike, as expected, at the top of the liquid cloud layer, reaching values of $-0.15$, $-0.5$ and $-0.15$ K h$^{-1}$ over the ocean, MIZ and sea-ice, respectively. The variability over ocean and sea-ice in the radiative cooling rates within the cloud layer is the largest, due to differences in cloud top height and/or temperature in those sections of the airmass transformation. Over the MIZ, the cloud developing within the boundary layer causes an additional local radiative cooling of $-0.05$ K h$^{-1}$.

Turbulent processes are also efficient in removing heat and moisture from the airmass, but their effect is confined within the boundary layer (Fig. 7b,e). Over the ocean, the turbulent heat loss is weaker, around $-$ 0.15 K h$^{-1}$ in the middle of the PBL and gradually dropping to zero the top. As the stratification becomes stronger, the turbulent cooling rates grow to $-0.4$ K h$^{-1}$ over the MIZ. While the turbulent cooling for the ocean and MIZ is more uniformly distributed within the PBL, over sea-ice the temperature tendency drops almost linearly with height, reaching a minimum of $-0.3$ K h$^{-1}$ near the PBL top.

$\frac{\partial T}{\partial t}_{TURB}$ turns weakly positive (around $-0.05$ K h$^{-1}$) near the surface for all legs. This could be in response to the near surface cooling induced by radiation (Fig. 7a) and dynamics (Fig. 7d). Turbulence induced by radiative cooling at the cloud top mostly redistributes heat and moisture within the cloud layer, more prominently over the MIZ where cloud liquid water content and cloud top radiative cooling are, on average, largest. Turbulent tendencies, as well as fluxes (not shown), of both heat and moisture drop to zero near cloud base. This is an indication that the cloud layer, as defined here, is generally decoupled from the surface and has no part in the overturning of the boundary layer and the consequent downward mixing of heat and moisture. With the exception of the time the airmass spends over the MIZ when new cloud formation occurs within the boundary layer, the rest of the time, turbulent fluxes near the surface are solely mechanically driven.

Turbulent processes appear to be consistently depleting the airmass of its moisture throughout the transformation (Fig. 7e), even over ocean. While it is possible for moisture deposition to temporarily occur over aquatic surfaces, we consider the magnitude and persistence of it in our AOSCM simulations and ERA5 (Fig. 3h) to be overestimated. A potential explanation for this overestimation could be the excessive downward mixing of heat and moisture by the IFS PBL scheme in stable conditions (Sandu et al., 2013; Holtslag et al., 2013).

The AOSCM cloud scheme drives changes in the airmass temperature and moisture through the release and consumption of latent heat during evaporation and condensation processes (Fig. 7c,f). During the oceanic leg of the airmass transformation, the cloud varies little, with weakly positive mean tendencies in the top part of the cloud layer, due to some overall small cloud liquid water growth, and negative tendencies towards the cloud base, due to evaporation of precipitation. The liquid cloud grows over the MIZ, possibly due to the enhanced radiative cooling at the time, while a new cloud layer is formed in the boundary layer, where the condensation related temperature tendencies, equal to 0.1 K h$^{-1}$ partially offsetting the radiative and turbulent cooling. In the residual layer, small peaks in $\frac{\partial T}{\partial t}_{CLOUD}$ show small changes in the overlying ice cloud. Over sea-ice, the cloud scheme produces major warming, as high as 0.3 K h$^{-1}$, for both the boundary and the overlying liquid cloud layers.

The dynamic tendencies of temperature ($\frac{\partial T}{\partial t}_{DYN}$, Fig. 7d), and moisture ($\frac{\partial q}{\partial t}_{DYN}$, Fig. 7g) in the absence of horizontal advection as required in this Lagrangian single-column framework, represents both vertical transport and the adiabatic temperature changes that comes as a result of the prescribed subsidence conditions. Over the ocean, the adiabatic tendencies are mostly insignificant. The median profiles showing minor warming (0.05 K h$^{-1}$) over the top half of the boundary layer, po-

https://doi.org/10.5194/egusphere-2024-3709
Preprint. Discussion started: 13 January 2025


tentially corresponding to the consistent low-level large-scale subsidence pulse shown in Fig. 5p while. Closer to the surface, $\frac{\partial T}{\partial t}_{DYN}$ turns slightly negative ($-0.005$ K h$^{-1}$). Over the MIZ, $\frac{\partial T}{\partial t}_{DYN}$ changes sign again, on average cooling the boundary layer by 0.1 K h$^{-1}$ while weakly warming the cloud layer by 0.05 K h$^{-1}$. However, the 75th percentile reaches up to 0.5 K h$^{-1}$ at the top of the cloud layer. In the MIZ, the cloud takes up larger part of the 5 km layer, making the effect of the adiabatic warming more significant and explaining the change of slope in the $\overline{T}_{5km}$~IWV$_{5km}$ diagram (Fig. 4). The strong upward motion over the sea-ice leg (Fig. 5p) results in a strong adiabatic cooling throughout the airmass, with the inversions at the top of the boundary and liquid cloud layer, once again being the most sensitive to the temperature changes induced by the vertical motion. Adiabatic cooling appears to be responsible for the accelerated loss of heat within the airmass over sea-ice, as well as moisture, considering the mirroring appearances of $\frac{\partial T}{\partial t}_{DYN}$ and $\frac{\partial T}{\partial t}_{CLOUD}$, with the latter showing rapid condensation in response to large-scale updrafts, that depletes of the moisture content of the airmass.

## 4 Conclusions

We studied the airmass transformation of a mid-April warm-air intrusion (WAI) using Lagrangian single-column simulations and observations collected by the 2022 HALO-$(\mathcal{AC})^3$ aircraft campaign. Our trajectory analysis of the WAI event is in agreement with the findings of Svensson et al. (2023); air parcels transported at different heights within a 5 km deep column align vertically. Through further investigation using ERA5 reanalysis data, we were able to conclude that the aligned trajectories are representative of the advected airmass to a satisfactory degree. The airmass' ability to maintain a column-like structure throughout the WAI event motivated us to construct and apply a Lagrangian single-column modeling framework based on the Atmosphere-Ocean Single-Column Model (AOSCM, Hartung et al., 2018).

In our framework, advection is represented through the temporal changes in the surface and dynamical forcing. In addition, we use the aligned trajectories to perform ensemble simulations of the airmass transformation, thus incorporating the variability of the airmass properties as well as the different forcing scenarios the airmass realistically may be subjected to along its track. Comparing to observations, ERA5 reanalysis and IFS operational forecast data (IFS-OF), we found that the model is able to adequately reproduce the magnitude and timescales of the transformation, from the bulk changes in heat and moisture content to the evolution of the vertical thermodynamic and cloud structure. During the advection over ocean and in the absence of strong large-scale subsidence conditions, radiation and boundary layer processes deplete the airmass' heat content while over the MIZ, the moisture condenses into a multi-layer cloud. Deeper into the Arctic, large updrafts accelerated the heat loss through adiabatic cooling and consequently enhanced the drying response of cloud and precipitation processes.

The AOSCM struggled to represent the evolution of the stable boundary layer throughout the simulation. The demonstrated biases were, in part, expected due to the overly diffusive closure in stable conditions implemented in IFS (Sandu et al., 2013; Holtslag et al., 2013). Furthermore, our ensemble simulations revealed a large dependence on the forcing conditions, especially the along-track vertical air motion. The role of subsidence has not been adequately accounted for in the mostly idealized WAI airmass transformation modeling studies that have been attempted to date (Pithan et al., 2018). Part of the reason lies in the lack of observations and/or observational methods for the large-scale vertical motion, making reanalysis products, such as ERA5, the most common source for forcing information in SCM and LES experiments. The HALO-$(\mathcal{AC})^3$ campaign (Wendisch et al., 2024) attempted measuring the large-scale subsidence on multiple counts (Paulus et al., 2024), including a cold-air outbreak event. They found agreement between measurements and ERA5 reanalysis data to be inconsistent, showing significant mismatch in the magnitude and even sign of vertical velocity ($\omega$). In this context, it is difficult to determine whether the prescribed subsidence profiles in our simulations and their consequent impact of the airmass transformation is realistic. Another caution could be our Lagrangian framework's simplifications, such as the exclusion of trajectories within the boundary layer and the abrupt transitions between the different surface regimes.

In conclusion, our Lagrangian AOSCM framework is a novel tool that facilitates the simulation of realistic WAI events and, therefore, the direct evaluation with observations and can virtually be applied to simulate any case of meridional airmass transport. The use of the model on a wide range of warm-air intrusions and cold-air outbreak events that have been captured over time by ship and aircraft experimental campaigns would be a valuable source of information in identifying common features between the respective airmass transformations and uncovering persistent model biases. The AOSCM shares the same physical parameterizations as in EC-Earth and OpenIFS and, according to our results, is able to reconstruct an airmass transformation similar to its global equivalent. A more expansive study using the Lagrangian AOSCM framework could be used for the mitigation of long-standing parameterization deficiencies related to the airmass transformation and consequently the Arctic climate, conducing to a long-term benefit for weather forecasts and climate projections.

*Code and data availability.* All data collected during the HALO–$(\mathcal{AC})^3$ aircraft campaign are being published by Ehrlich et al. (2024) . Users of the AOSCM are required to be affiliated with an institution that is a member of the EC-Earth consortium (http://www.ec-earth.org, last access: 26 November 2024) and has acquired an OpenIFS license agreement from ECMWF (https://confluence.ecmwf.int/display/OIFS/OpenIFS+Licensing, last access: 26 November 2024). The Lagrangian AOSCM source code can be found on used for the results presented here can be downloaded from the EC-Earth development portal: https://svn.ec-earth.org/ecearth3/branches/development/2016/r2740-coupled-SCM/branches/lagrangian (last access: 26 November 2025). Revision 10327 was used for the results presented in this study. The ERA5 data used for forcing and initialization of the AOSCM, as well as model output can be found at: (bolin center data base; application still in process, DOI not available yet). Codes and scripts for performing the analyses and plotting are available on request from the authors.

*Author contributions.* MK and GS developed the research ideas and designed the study. MK, in continuous discussions with GS, constructed the Lagrangian modeling framework. MK performed the simulations and analysis and created an initial draft of the manuscript. GS, MW and MT contributed substantial improvements to the final version of the manuscript with their meaningful feedback and suggestions.

*Competing interests.* Some authors are members of the editorial board of Atmospheric Chemistry and Physics.

https://doi.org/10.5194/egusphere-2024-3709
Preprint. Discussion started: 13 January 2025


*Acknowledgements.* We gratefully acknowledge support from the Swedish Research Council (VR, project 2020-04064) as well as the funding by the Deutsche Forschungsgemeinschaft (DFG, German Research Foundation) – Project Number 268020496 – TRR 172, within the framework of the Transregional Collaborative Research Center "ArctiC Amplification: Climate Relevant Atmospheric and SurfaCe Processes, and Feedback Mechanisms (AC)3". We are further thankful for funding of project grant no. 316646266 by DFG within the framework of Priority Programme SPP 1294 to promote research with HALO. We thank the PIs Susanne Crewell, Felix Pithan and all involved in planning and executing the research flights as well as the pilots technicians that operated the aircrafts. We further acknowledge the efforts of Henning Dorff, Benjamin Kirbus and Marlen Brückner in collecting the dropsonde measurements used in this study, as well as Geet George for curating the dropsonde dataset. The computations and data handling were enabled by resources provided by the National Academic Infrastructure for Supercomputing in Sweden (NAISS), partially funded by the Swedish Research Council through grant agreement no. 2022-06725.

https://doi.org/10.5194/egusphere-2024-3709
Preprint. Discussion started: 13 January 2025


## References

Ali, S. M. and Pithan, F.: Following moist intrusions into the Arctic using SHEBA observations in a Lagrangian perspective, Quarterly Journal of the Royal Meteorological Society, 146, 3522–3533, https://doi.org/10.1002/qj.3859, _eprint: https://onlinelibrary.wiley.com/doi/pdf/10.1002/qj.3859, 2020.

Cohen, L., Hudson, S. R., Walden, V. P., Graham, R. M., and Granskog, M. A.: Meteorological conditions in a thinner Arctic sea ice regime from winter to summer during the Norwegian Young Sea Ice expedition (N-ICE2015), Journal of Geophysical Research: Atmospheres, 122, 7235–7259, https://doi.org/10.1002/2016JD026034, _eprint: https://onlinelibrary.wiley.com/doi/pdf/10.1002/2016JD026034, 2017.

Cronin, T. W. and Tziperman, E.: Low clouds suppress Arctic air formation and amplify high-latitude continental winter warming, Proceedings of the National Academy of Sciences, 112, 11 490–11 495, https://doi.org/10.1073/pnas.1510937112, publisher: Proceedings of the National Academy of Sciences, 2015.

Curry, J.: On the Formation of Continental Polar Air, Journal of the Atmospheric Sciences, 40, 2278–2292, https://doi.org/10.1175/1520-0469(1983)040<2278:OTFOCP>2.0.CO;2, publisher: American Meteorological Society Section: Journal of the Atmospheric Sciences, 1983.

Dimitrelos, A., Caballero, R., and Ekman, A. M. L.: Controls on Surface Warming by Winter Arctic Moist Intrusions in Idealized Large-Eddy Simulations, Journal of Climate, 36, 1287–1300, https://doi.org/10.1175/JCLI-D-22-0174.1, publisher: American Meteorological Society Section: Journal of Climate, 2023.

Döscher, R., Acosta, M., Alessandri, A., Anthoni, P., Arsouze, T., Bergman, T., Bernardello, R., Boussetta, S., Caron, L.-P., Carver, G., Castrillo, M., Catalano, F., Cvijanovic, I., Davini, P., Dekker, E., Doblas-Reyes, F. J., Docquier, D., Echevarria, P., Fladrich, U., Fuentes-Franco, R., Gröger, M., v. Hardenberg, J., Hieronymus, J., Karami, M. P., Keskinen, J.-P., Koenigk, T., Makkonen, R., Massonnet, F., Ménégoz, M., Miller, P. A., Moreno-Chamarro, E., Nieradzik, L., van Noije, T., Nolan, P., O'Donnell, D., Ollinaho, P., van den Oord, G., Ortega, P., Prims, O. T., Ramos, A., Reerink, T., Rousset, C., Ruprich-Robert, Y., Le Sager, P., Schmith, T., Schrödner, R., Serva, F., Sicardi, V., Sloth Madsen, M., Smith, B., Tian, T., Tourigny, E., Uotila, P., Vancoppenolle, M., Wang, S., Wårlind, D., Willén, U., Wyser, K., Yang, S., Yepes-Arbós, X., and Zhang, Q.: The EC-Earth3 Earth system model for the Coupled Model Intercomparison Project 6, Geoscientific Model Development, 15, 2973–3020, https://doi.org/10.5194/gmd-15-2973-2022, publisher: Copernicus GmbH, 2022.

Ehrlich, A., Wendisch, M., Lüpkes, C., Buschmann, M., Bozem, H., Chechin, D., Clemen, H.-C., Dupuy, R., Eppers, O., Hartmann, J., Herber, A., Jäkel, E., Järvinen, E., Jourdan, O., Kästner, U., Kliesch, L.-L., Köllner, F., Mech, M., Mertes, S., Neuber, R., Ruiz-Donoso, E., Schnaiter, M., Schneider, J., Stapf, J., and Zanatta, M.: A comprehensive in situ and remote sensing data set from the Arctic CLoud Observations Using airborne measurements during polar Day (ACLOUD) campaign, Earth System Science Data, 11, 1853–1881, https://doi.org/10.5194/essd-11-1853-2019, publisher: Copernicus GmbH, 2019.

Ehrlich, A., Crewell, S., Herber, A., Klingebiel, M., Lüpkes, C., Mech, M., Becker, S., Borrmann, S., Bozem, H., Buschmann, M., Clemen, H.-C., De La Torre Castro, E., Dorff, H., Dupuy, R., Eppers, O., Ewald, F., George, G., Giez, A., Grawe, S., Gourbeyre, C., Hartmann, J., Jäkel, E., Joppe, P., Jourdan, O., Jurányi, Z., Kirbus, B., Lucke, J., Luebke, A. E., Maahn, M., Maherndl, N., Mallaun, C., Mayer, J., Mertes, S., Mioche, G., Moser, M., Müller, H., Pörtge, V., Risse, N., Roberts, G., Rosenburg, S., Röttenbacher, J., Schäfer, M., Schaefer, J., Schäfler, A., Schirmacher, I., Schneider, J., Schnitt, S., Stratmann, F., Tatzelt, C., Voigt, C., Walbröl, A., Weber, A., Wetzel, B., Wirth, M., and Wendisch, M.: A comprehensive in-situ and remote sensing data set collected during the HALO–(AC)$^3$ aircraft campaign, Earth System Science Data Discussions, pp. 1–49, https://doi.org/10.5194/essd-2024-281, publisher: Copernicus GmbH, 2024.

https://doi.org/10.5194/egusphere-2024-3709
Preprint. Discussion started: 13 January 2025


Fitch, A. C.: Improving stratocumulus cloud turbulence and entrainment parametrizations in OpenIFS, Quarterly Journal of the Royal Meteorological Society, 148, 1782–1804, https://doi.org/10.1002/qj.4278, _eprint: https://onlinelibrary.wiley.com/doi/pdf/10.1002/qj.4278, 2022.

Gascard, J.-C., Festy, J., le Goff, H., Weber, M., Bruemmer, B., Offermann, M., Doble, M., Wadhams, P., Forsberg, R., Hanson, S., Skourup, H., Gerland, S., Nicolaus, M., Metaxian, J.-P., Grangeon, J., Haapala, J., Rinne, E., Haas, C., Wegener, A., Heygster, G., Jakobson, E., Palo, T., Wilkinson, J., Kaleschke, L., Claffey, K., Elder, B., and Bottenheim, J.: Exploring Arctic Transpolar Drift During Dramatic Sea Ice Retreat, Eos, Transactions American Geophysical Union, 89, 21–22, https://doi.org/10.1029/2008EO030001, _eprint: https://onlinelibrary.wiley.com/doi/pdf/10.1029/2008EO030001, 2008.

Goosse, H., Kay, J. E., Armour, K. C., Bodas-Salcedo, A., Chepfer, H., Docquier, D., Jonko, A., Kushner, P. J., Lecomte, O., Massonnet, F., Park, H.-S., Pithan, F., Svensson, G., and Vancoppenolle, M.: Quantifying climate feedbacks in polar regions, Nature Communications, 9, 1919, https://doi.org/10.1038/s41467-018-04173-0, number: 1 Publisher: Nature Publishing Group, 2018.

Gorodetskaya, I. V., Tsukernik, M., Claes, K., Ralph, M. F., Neff, W. D., and Van Lipzig, N. P. M.: The role of atmospheric rivers in anomalous snow accumulation in East Antarctica, Geophysical Research Letters, 41, 6199–6206, https://doi.org/10.1002/2014GL060881, _eprint: https://onlinelibrary.wiley.com/doi/pdf/10.1002/2014GL060881, 2014.

Graham, R. M., Cohen, L., Ritzhaupt, N., Segger, B., Graversen, R. G., Rinke, A., Walden, V. P., Granskog, M. A., and Hudson, S. R.: Evaluation of Six Atmospheric Reanalyses over Arctic Sea Ice from Winter to Early Summer, https://doi.org/10.1175/JCLI-D-18-0643.1, section: Journal of Climate, 2019.

Guan, B. and Waliser, D. E.: Detection of atmospheric rivers: Evaluation and application of an algorithm for global studies, Journal of Geophysical Research: Atmospheres, 120, 12 514–12 535, https://doi.org/10.1002/2015JD024257, _eprint: https://onlinelibrary.wiley.com/doi/pdf/10.1002/2015JD024257, 2015.

Hartung, K., Svensson, G., Struthers, H., Deppenmeier, A.-L., and Hazeleger, W.: An EC-Earth coupled atmosphere–ocean single-column model (AOSCM.v1_EC-Earth3) for studying coupled marine and polar processes, Geoscientific Model Development, 11, 4117–4137, https://doi.org/10.5194/gmd-11-4117-2018, publisher: Copernicus GmbH, 2018.

Hartung, K., Svensson, G., Holt, J., Lewinschal, A., and Tjernström, M.: Exploring the Dynamics of an Arctic Sea Ice Melt Event Using a Coupled Atmosphere-Ocean Single-Column Model (AOSCM), Journal of Advances in Modeling Earth Systems, 14, e2021MS002 593, https://doi.org/10.1029/2021MS002593, _eprint: https://onlinelibrary.wiley.com/doi/pdf/10.1029/2021MS002593, 2022.

Herman, G. and Goody, R.: Formation and Persistence of Summertime Arctic Stratus Clouds, Journal of the Atmospheric Sciences, 33, 1537–1553, https://doi.org/10.1175/1520-0469(1976)033<1537:FAPOSA>2.0.CO;2, publisher: American Meteorological Society Section: Journal of the Atmospheric Sciences, 1976.

Hersbach, H., Bell, B., Berrisford, P., Hirahara, S., Horányi, A., Muñoz-Sabater, J., Nicolas, J., Peubey, C., Radu, R., Schepers, D., Simmons, A., Soci, C., Abdalla, S., Abellan, X., Balsamo, G., Bechtold, P., Biavati, G., Bidlot, J., Bonavita, M., De Chiara, G., Dahlgren, P., Dee, D., Diamantakis, M., Dragani, R., Flemming, J., Forbes, R., Fuentes, M., Geer, A., Haimberger, L., Healy, S., Hogan, R. J., Hólm, E., Janisková, M., Keeley, S., Laloyaux, P., Lopez, P., Lupu, C., Radnoti, G., de Rosnay, P., Rozum, I., Vamborg, F., Villaume, S., and Thépaut, J.-N.: The ERA5 global reanalysis, Quarterly Journal of the Royal Meteorological Society, 146, 1999–2049, https://doi.org/10.1002/qj.3803, _eprint: https://onlinelibrary.wiley.com/doi/pdf/10.1002/qj.3803, 2020.

Holtslag, A. a. M., Svensson, G., Baas, P., Basu, S., Beare, B., Beljaars, A. C. M., Bosveld, F. C., Cuxart, J., Lindvall, J., Steeneveld, G. J., Tjernström, M., and Wiel, B. J. H. V. D.: Stable Atmospheric Boundary Layers and Diurnal Cycles: Challenges for Weather and Climate Models, https://doi.org/10.1175/BAMS-D-11-00187.1, section: Bulletin of the American Meteorological Society, 2013.

https://doi.org/10.5194/egusphere-2024-3709
Preprint. Discussion started: 13 January 2025


Klein, S. A., McCoy, R. B., Morrison, H., Ackerman, A. S., Avramov, A., Boer, G. d., Chen, M., Cole, J. N. S., Del Genio, A. D., Falk, M., Foster, M. J., Fridlind, A., Golaz, J.-C., Hashino, T., Harrington, J. Y., Hoose, C., Khairoutdinov, M. F., Larson, V. E., Liu, X., Luo, Y., McFarquhar, G. M., Menon, S., Neggers, R. A. J., Park, S., Poellot, M. R., Schmidt, J. M., Sednev, I., Shipway, B. J., Shupe, M. D., Spangenberg, D. A., Sud, Y. C., Turner, D. D., Veron, D. E., Salzen, K. v., Walker, G. K., Wang, Z., Wolf, A. B., Xie, S., Xu, K.-M., Yang, F., and Zhang, G.: Intercomparison of model simulations of mixed-phase clouds observed during the ARM Mixed-Phase Arctic Cloud Experiment. I: single-layer cloud, Quarterly Journal of the Royal Meteorological Society, 135, 979–1002, https://doi.org/10.1002/qj.416, _eprint: https://onlinelibrary.wiley.com/doi/pdf/10.1002/qj.416, 2009.

Mech, M., Ehrlich, A., Herber, A., Lüpkes, C., Wendisch, M., Becker, S., Boose, Y., Chechin, D., Crewell, S., Dupuy, R., Gourbeyre, C., Hartmann, J., Jäkel, E., Jourdan, O., Kliesch, L.-L., Klingebiel, M., Kulla, B. S., Mioche, G., Moser, M., Risse, N., Ruiz-Donoso, E., Schäfer, M., Stapf, J., and Voigt, C.: MOSAiC-ACA and AFLUX - Arctic airborne campaigns characterizing the exit area of MOSAiC, Scientific Data, 9, 790, https://doi.org/10.1038/s41597-022-01900-7, publisher: Nature Publishing Group, 2022.

Mirocha, J. D. and Kosović, B.: A Large-Eddy Simulation Study of the Influence of Subsidence on the Stably Stratified Atmospheric Boundary Layer, Boundary-Layer Meteorology: An International Journal of Physical, Chemical and Biological Processes in the Atmospheric Boundary Layer, 134, https://doi.org/10.1007/s10546-009-9449-4, 2010.

Morrison, H., de Boer, G., Feingold, G., Harrington, J., Shupe, M. D., and Sulia, K.: Resilience of persistent Arctic mixed-phase clouds, Nature Geoscience, 5, 11–17, https://doi.org/10.1038/ngeo1332, number: 1 Publisher: Nature Publishing Group, 2012.

Murto, S., Caballero, R., Svensson, G., and Papritz, L.: Interaction between Atlantic cyclones and Eurasian atmospheric blocking drives wintertime warm extremes in the high Arctic, Weather and Climate Dynamics, 3, 21–44, https://doi.org/10.5194/wcd-3-21-2022, publisher: Copernicus GmbH, 2022.

Neggers, R. a. J.: Attributing the behavior of low-level clouds in large-scale models to subgrid-scale parameterizations, Journal of Advances in Modeling Earth Systems, 7, 2029–2043, https://doi.org/10.1002/2015MS000503, _eprint: https://onlinelibrary.wiley.com/doi/pdf/10.1002/2015MS000503, 2015.

Papritz, L., Hauswirth, D., and Hartmuth, K.: Moisture origin, transport pathways, and driving processes of intense wintertime moisture transport into the Arctic, Weather and Climate Dynamics, 3, 1–20, https://doi.org/10.5194/wcd-3-1-2022, publisher: Copernicus GmbH, 2022.

Paulus, F. M., Karalis, M., George, G., Svensson, G., Wendisch, M., and Neggers, R. A. J.: Airborne measurements of mesoscale divergence at high latitudes during HALO-(AC)3, https://doi.org/10.1175/JAS-D-24-0034.1, section: Journal of the Atmospheric Sciences, 2024.

Perovich, D. K., Andreas, E. L., Curry, J. A., Eiken, H., Fairall, C. W., Grenfell, T. C., Guest, P., Intrieri, J., Kadko, D., Lindsay, R. W., McPhee, M. G., Morison, J., Moritz, R. E., Paulson, C. A., Pegau, W. S., Persson, P., Pinkel, R., Richter-Menge, J. A., Stanton, T., Stern, H., Sturm, M., Tucker III, W., and Uttal, T.: Year on ice gives climate insights, Eos, Transactions American Geophysical Union, 80, 481–486, https://doi.org/10.1029/EO080i041p00481-01, _eprint: https://onlinelibrary.wiley.com/doi/pdf/10.1029/EO080i041p00481-01, 1999.

Pithan, F. and Mauritsen, T.: Arctic amplification dominated by temperature feedbacks in contemporary climate models, Nature Geoscience, 7, 181–184, https://doi.org/10.1038/ngeo2071, number: 3 Publisher: Nature Publishing Group, 2014.

Pithan, F., Ackerman, A., Angevine, W. M., Hartung, K., Ickes, L., Kelley, M., Medeiros, B., Sandu, I., Steeneveld, G.-J., Sterk, H. a. M., Svensson, G., Vaillancourt, P. A., and Zadra, A.: Select strengths and biases of models in representing the Arctic winter boundary layer over sea ice: the Larcform 1 single column model intercomparison, Journal of Advances in Modeling Earth Systems, 8, 1345–1357, https://doi.org/10.1002/2016MS000630, _eprint: https://onlinelibrary.wiley.com/doi/pdf/10.1002/2016MS000630, 2016.

https://doi.org/10.5194/egusphere-2024-3709
Preprint. Discussion started: 13 January 2025


Pithan, F., Svensson, G., Caballero, R., Chechin, D., Cronin, T. W., Ekman, A. M. L., Neggers, R., Shupe, M. D., Solomon, A., Tjernström, M., and Wendisch, M.: Role of air-mass transformations in exchange between the Arctic and mid-latitudes, Nature Geoscience, 11, 805–812, https://doi.org/10.1038/s41561-018-0234-1, number: 11 Publisher: Nature Publishing Group, 2018.

Rantanen, M., Karpechko, A. Y., Lipponen, A., Nordling, K., Hyvärinen, O., Ruosteenoja, K., Vihma, T., and Laaksonen, A.: The Arctic has warmed nearly four times faster than the globe since 1979, Communications Earth & Environment, 3, 1–10, https://doi.org/10.1038/s43247-022-00498-3, number: 1 Publisher: Nature Publishing Group, 2022.

Rousset, C., Vancoppenolle, M., Madec, G., Fichefet, T., Flavoni, S., Barthélemy, A., Benshila, R., Chanut, J., Levy, C., Masson, S., and Vivier, F.: The Louvain-La-Neuve sea ice model LIM3.6: global and regional capabilities, Geoscientific Model Development, 8, 2991–3005, https://doi.org/10.5194/gmd-8-2991-2015, publisher: Copernicus GmbH, 2015.

Sandu, I., Beljaars, A., Bechtold, P., Mauritsen, T., and Balsamo, G.: Why is it so difficult to represent stably stratified conditions in numerical weather prediction (NWP) models?, Journal of Advances in Modeling Earth Systems, 5, 117–133, https://doi.org/10.1002/jame.20013, _eprint: https://onlinelibrary.wiley.com/doi/pdf/10.1002/jame.20013, 2013.

Serreze, M. C., Walsh, J. E., Chapin, F. S., Osterkamp, T., Dyurgerov, M., Romanovsky, V., Oechel, W. C., Morison, J., Zhang, T., and Barry, R. G.: Observational Evidence of Recent Change in the Northern High-Latitude Environment, Climatic Change, 46, 159–207, https://doi.org/10.1023/A:1005504031923, 2000.

Shupe, M. D., Rex, M., Blomquist, B., Persson, P. O. G., Schmale, J., Uttal, T., Althausen, D., Angot, H., Archer, S., Bariteau, L., Beck, I., Bilberry, J., Bucci, S., Buck, C., Boyer, M., Brasseur, Z., Brooks, I. M., Calmer, R., Cassano, J., Castro, V., Chu, D., Costa, D., Cox, C. J., Creamean, J., Crewell, S., Dahlke, S., Damm, E., de Boer, G., Deckelmann, H., Dethloff, K., Dütsch, M., Ebell, K., Ehrlich, A., Ellis, J., Engelmann, R., Fong, A. A., Frey, M. M., Gallagher, M. R., Ganzeveld, L., Gradinger, R., Graeser, J., Greenamyer, V., Griesche, H., Griffiths, S., Hamilton, J., Heinemann, G., Helmig, D., Herber, A., Heuzé, C., Hofer, J., Houchens, T., Howard, D., Inoue, J., Jacobi, H.-W., Jaiser, R., Jokinen, T., Jourdan, O., Jozef, G., King, W., Kirchgaessner, A., Klingebiel, M., Krassovski, M., Krumpen, T., Lampert, A., Landing, W., Laurila, T., Lawrence, D., Lonardi, M., Loose, B., Lüpkes, C., Maahn, M., Macke, A., Maslowski, W., Marsay, C., Maturilli, M., Mech, M., Morris, S., Moser, M., Nicolaus, M., Ortega, P., Osborn, J., Pätzold, F., Perovich, D. K., Petäjä, T., Pilz, C., Pirazzini, R., Posman, K., Powers, H., Pratt, K. A., Preußer, A., Quéléver, L., Radenz, M., Rabe, B., Rinke, A., Sachs, T., Schulz, A., Siebert, H., Silva, T., Solomon, A., Sommerfeld, A., Spreen, G., Stephens, M., Stohl, A., Svensson, G., Uin, J., Viegas, J., Voigt, C., von der Gathen, P., Wehner, B., Welker, J. M., Wendisch, M., Werner, M., Xie, Z., and Yue, F.: Overview of the MOSAiC expedition: Atmosphere, Elementa: Science of the Anthropocene, 10, 00 060, https://doi.org/10.1525/elementa.2021.00060, 2022.

Solomon, A., Shupe, M. D., Persson, O., Morrison, H., Yamaguchi, T., Caldwell, P. M., and De Boer, G.: The Sensitivity of Springtime Arctic Mixed-Phase Stratocumulus Clouds to Surface-Layer and Cloud-Top Inversion-Layer Moisture Sources, Journal of the Atmospheric Sciences, 71, 574–595, https://doi.org/10.1175/JAS-D-13-0179.1, 2014.

Sprenger, M. and Wernli, H.: The LAGRANTO Lagrangian analysis tool – version 2.0, Geoscientific Model Development, 8, 2569–2586, https://doi.org/10.5194/gmd-8-2569-2015, publisher: Copernicus GmbH, 2015.

Svensson, G. and Karlsson, J.: On the Arctic Wintertime Climate in Global Climate Models, Journal of Climate, 24, 5757–5771, https://doi.org/10.1175/2011JCLI4012.1, publisher: American Meteorological Society Section: Journal of Climate, 2011.

Svensson, G., Murto, S., Shupe, M. D., Pithan, F., Magnusson, L., Day, J. J., Doyle, J. D., Renfrew, I. A., Spengler, T., and Vihma, T.: Warm air intrusions reaching the MOSAiC expedition in April 2020—The YOPP targeted observing period (TOP), Elem Sci Anth, 11, 00 016, https://doi.org/10.1525/elementa.2023.00016, 2023.

https://doi.org/10.5194/egusphere-2024-3709
Preprint. Discussion started: 13 January 2025


Taylor, P. C., Boeke, R. C., Boisvert, L. N., Feldl, N., Henry, M., Huang, Y., Langen, P. L., Liu, W., Pithan, F., Sejas, S. A., and Tan, I.: Process Drivers, Inter-Model Spread, and the Path Forward: A Review of Amplified Arctic Warming, Frontiers in Earth Science, 9, https://www.frontiersin.org/articles/10.3389/feart.2021.758361, 2022.

Tjernström, M., Leck, C., Birch, C. E., Bottenheim, J. W., Brooks, B. J., Brooks, I. M., Bäcklin, L., Chang, R. Y.-W., de Leeuw, G., Di Liberto, L., de la Rosa, S., Granath, E., Graus, M., Hansel, A., Heintzenberg, J., Held, A., Hind, A., Johnston, P., Knulst, J., Martin, M., Matrai, P. A., Mauritsen, T., Müller, M., Norris, S. J., Orellana, M. V., Orsini, D. A., Paatero, J., Persson, P. O. G., Gao, Q., Rauschenberg, C., Ristovski, Z., Sedlar, J., Shupe, M. D., Sierau, B., Sirevaag, A., Sjogren, S., Stetzer, O., Swietlicki, E., Szczodrak, M., Vaattovaara, P., Wahlberg, N., Westberg, M., and Wheeler, C. R.: The Arctic Summer Cloud Ocean Study (ASCOS): overview and experimental design, Atmospheric Chemistry and Physics, 14, 2823–2869, https://doi.org/10.5194/acp-14-2823-2014, publisher: Copernicus GmbH, 2014.

van Der Linden, S., Edwards, J., van Heerwaarden, C., Vignon, E., Genthon, C., Petenko, I., Baas, P., Jonker, H., and van de Wiel, B.: Large-Eddy Simulations of the Steady Wintertime Antarctic Boundary Layer, Boundary-Layer Meteorology, 173, 165–192, https://doi.org/10.1007/s10546-019-00461-4, publisher: Springer Verlag, 2019.

Vüllers, J., Achtert, P., Brooks, I. M., Tjernström, M., Prytherch, J., Burzik, A., and Neely III, R.: Meteorological and cloud conditions during the Arctic Ocean 2018 expedition, Atmospheric Chemistry and Physics, 21, 289–314, https://doi.org/10.5194/acp-21-289-2021, publisher: Copernicus GmbH, 2021.

Walbröl, A., Michaelis, J., Becker, S., Dorff, H., Ebell, K., Gorodetskaya, I., Heinold, B., Kirbus, B., Lauer, M., Maherndl, N., Maturilli, M., Mayer, J., Müller, H., Neggers, R. A. J., Paulus, F. M., Röttenbacher, J., Rückert, J. E., Schirmacher, I., Slättberg, N., Ehrlich, A., Wendisch, M., and Crewell, S.: Contrasting extremely warm and long-lasting cold air anomalies in the North Atlantic sector of the Arctic during the HALO-$(\mathcal{AC})^3$ campaign, Atmospheric Chemistry and Physics, 24, 8007–8029, https://doi.org/10.5194/acp-24-8007-2024, publisher: Copernicus GmbH, 2024.

Wendisch, M., Macke, A., Ehrlich, A., Lüpkes, C., Mech, M., Chechin, D., Dethloff, K., Velasco, C. B., Bozem, H., Brückner, M., Clemen, H.-C., Crewell, S., Donth, T., Dupuy, R., Ebell, K., Egerer, U., Engelmann, R., Engler, C., Eppers, O., Gehrmann, M., Gong, X., Gottschalk, M., Gourbeyre, C., Griesche, H., Hartmann, J., Hartmann, M., Heinold, B., Herber, A., Herrmann, H., Heygster, G., Hoor, P., Jafariserajehlou, S., Jäkel, E., Järvinen, E., Jourdan, O., Kästner, U., Kecorius, S., Knudsen, E. M., Köllner, F., Kretzschmar, J., Lelli, L., Leroy, D., Maturilli, M., Mei, L., Mertes, S., Mioche, G., Neuber, R., Nicolaus, M., Nomokonova, T., Notholt, J., Palm, M., Pinxteren, M. v., Quaas, J., Richter, P., Ruiz-Donoso, E., Schäfer, M., Schmieder, K., Schnaiter, M., Schneider, J., Schwarzenböck, A., Seifert, P., Shupe, M. D., Siebert, H., Spreen, G., Stapf, J., Stratmann, F., Vogl, T., Welti, A., Wex, H., Wiedensohler, A., Zanatta, M., and Zeppenfeld, S.: The Arctic Cloud Puzzle: Using ACLOUD/PASCAL Multiplatform Observations to Unravel the Role of Clouds and Aerosol Particles in Arctic Amplification, Bulletin of the American Meteorological Society, 100, 841–871, https://doi.org/10.1175/BAMS-D-18-0072.1, publisher: American Meteorological Society Section: Bulletin of the American Meteorological Society, 2019.

Wendisch, M., Crewell, S., Ehrlich, A., Herber, A., Kirbus, B., Lüpkes, C., Mech, M., Abel, S. J., Akansu, E. F., Ament, F., Aubry, C., Becker, S., Borrmann, S., Bozem, H., Brückner, M., Clemen, H.-C., Dahlke, S., Dekoutsidis, G., Delanoë, J., De La Torre Castro, E., Dorff, H., Dupuy, R., Eppers, O., Ewald, F., George, G., Gorodetskaya, I. V., Grawe, S., Groß, S., Hartmann, J., Henning, S., Hirsch, L., Jäkel, E., Joppe, P., Jourdan, O., Jurányi, Z., Karalis, M., Kellermann, M., Klingebiel, M., Lonardi, M., Lucke, J., Luebke, A. E., Maahn, M., Maherndl, N., Maturilli, M., Mayer, B., Mayer, J., Mertes, S., Michaelis, J., Michalkov, M., Mioche, G., Moser, M., Müller, H., Neggers, R., Ori, D., Paul, D., Paulus, F. M., Pilz, C., Pithan, F., Pöhlker, M., Pörtge, V., Ringel, M., Risse, N., Roberts, G. C., Rosenburg, S., Röttenbacher, J., Rückert, J., Schäfer, M., Schaefer, J., Schemann, V., Schirmacher, I., Schmidt, J., Schmidt, S., Schneider, J., Schnitt, S., Schwarz, A., Siebert, H., Sodemann, H., Sperzel, T., Spreen, G., Stevens, B., Stratmann, F., Svensson, G., Tatzelt, C., Tuch, T., Vihma, T.,

https://doi.org/10.5194/egusphere-2024-3709
Preprint. Discussion started: 13 January 2025


Voigt, C., Volkmer, L., Walbröl, A., Weber, A., Wehner, B., Wetzel, B., Wirth, M., and Zinner, T.: Overview: quasi-Lagrangian observations of Arctic air mass transformations – introduction and initial results of the HALO-($\mathcal{AC}$)$^3$ aircraft campaign, Atmospheric Chemistry and Physics, 24, 8865–8892, https://doi.org/10.5194/acp-24-8865-2024, publisher: Copernicus GmbH, 2024.

Wexler, H.: Cooling in the lower atmosphere and the structure of polar continental air, Monthly Weather Review, 64, 122 – 136, https://doi.org/10.1175/1520-0493(1936)64<122:CITLAA>2.0.CO;2, place: Boston MA, USA Publisher: American Meteorological Society, 1936.

Woods, C. and Caballero, R.: The Role of Moist Intrusions in Winter Arctic Warming and Sea Ice Decline, Journal of Climate, 29, 4473–4485, https://doi.org/10.1175/JCLI-D-15-0773.1, publisher: American Meteorological Society Section: Journal of Climate, 2016.

Woods, C., Caballero, R., and Svensson, G.: Large-scale circulation associated with moisture intrusions into the Arctic during winter, Geophysical Research Letters, 40, 4717–4721, https://doi.org/10.1002/grl.50912, _eprint: https://onlinelibrary.wiley.com/doi/pdf/10.1002/grl.50912, 2013.

Young, G., Connolly, P. J., Dearden, C., and Choularton, T. W.: Relating large-scale subsidence to convection development in Arctic mixed-phase marine stratocumulus, Atmospheric Chemistry and Physics, 18, 1475–1494, https://doi.org/10.5194/acp-18-1475-2018, publisher: Copernicus GmbH, 2018.

Zhou, W., Leung, L. R., Xie, S.-P., and Lu, J.: An analytic theory for the degree of Arctic Amplification, Nature Communications, 15, 5060, https://doi.org/10.1038/s41467-024-48469-w, publisher: Nature Publishing Group, 2024.

https://doi.org/10.5194/egusphere-2024-3709
Preprint. Discussion started: 13 January 2025


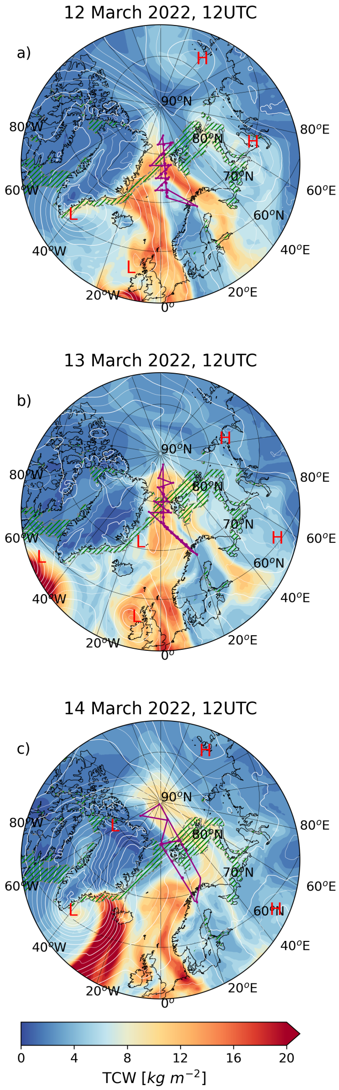


**Figure 1.** Maps of total column water (kg m$^{-2}$) at 12 UTC, on each day of the 12-14 March WAI event. Isobars between 940 hPa and 1080 hPa are plotted with thin(thick) white lines with a 5(10) hPa step. The centers of low and high pressure centers are marked with denoted with red letters. The green hatched area marks the extent of the marginal ice zone (MIZ) which corresponds to sea-ice fraction between values of 0 and 0.9. Purple lines represent the respective HALO flight tracks (RF02, RF03, RF04) over the North Atlantic. The purple dots correspond to the locations of dropsondes released during each flight.

https://doi.org/10.5194/egusphere-2024-3709
Preprint. Discussion started: 13 January 2025


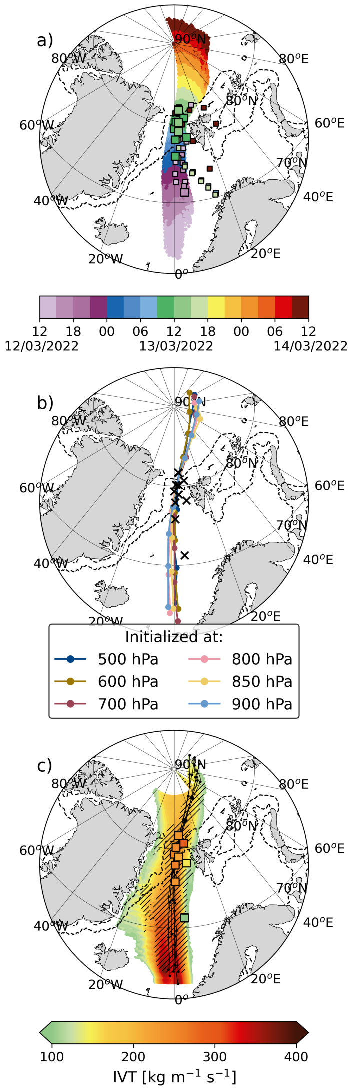


**Figure 2.** a) 24-hour long backward and forward trajectories initialized at pressure levels (500, 600, 700, 800, 850 and 900 hPa), within a 100 km-radius circle centered on 81 °N and 5 °E on 13 March, at 12 UTC (day of year = 72.5). The coloring along the trajectories represents the air-parcels' time of arrival at the marked location. The squares mark the locations of all dropsondes released during flights RF02, RF03 and RF04 and are tinted, similarly to the trajectories, according to the dropsonde launch. Smaller squares are used to denote observations whose location and time of launch constitutes the unfit for comparison with trajectories. Dashed contours show boundaries of the MIZ, corresponding to sea-ice concentration values 0 and 0.9, at the time of the trajectory initialization. b) The trajectory ensemble consisting of one trajectory per pressure level, colored accordingly. Dots mark 6 hour long periods. X-shaped markers show the locations of observed profiles suited for comparison. c) temporal evolution and spatial variability of integrated water vapor transport (IVT). The trajectory ensemble is shown with black lines. Hatches mark the correlation range (see Sect. 2.3 ) around the airmass at each timestep.

https://doi.org/10.5194/egusphere-2024-3709
Preprint. Discussion started: 13 January 2025


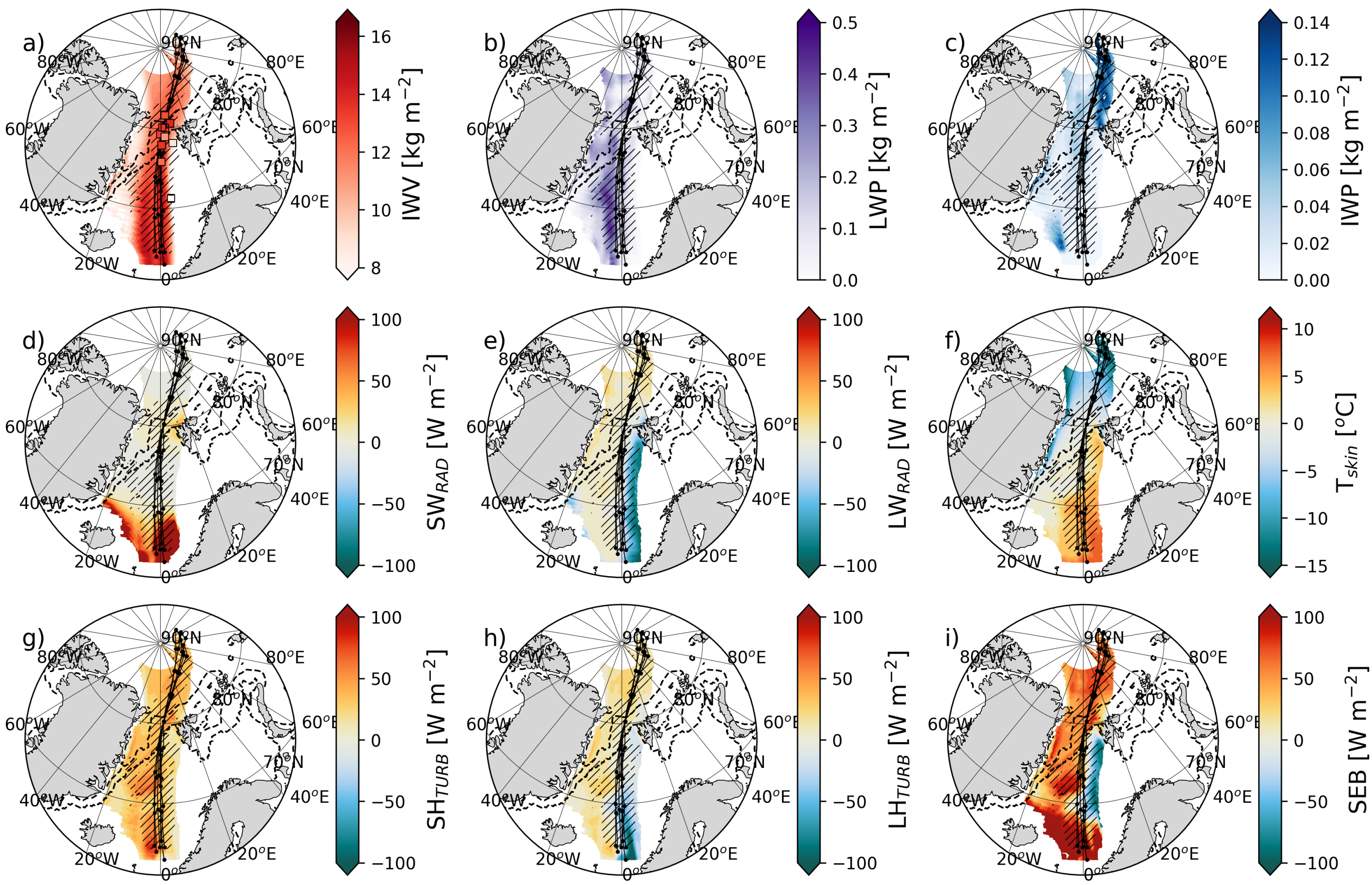


**Figure 3.** Temporal evolution and spatial variability of the airmass during its poleward advection in terms of specific water content of water vapor, liquid and ice cloud(a-c) and energy exchange at the surface (d-i). The trajectory ensemble is shown with black lines. Hatches mark the correlation range (see Sect. 2.3 ) around the airmass at each timestep. Square markers, when present, correspond to the observed values. Dashed contours show boundaries of the MIZ, corresponding to sea-ice concentration values 0 and 0.9 on March 13, at 12 UTC.

https://doi.org/10.5194/egusphere-2024-3709
Preprint. Discussion started: 13 January 2025


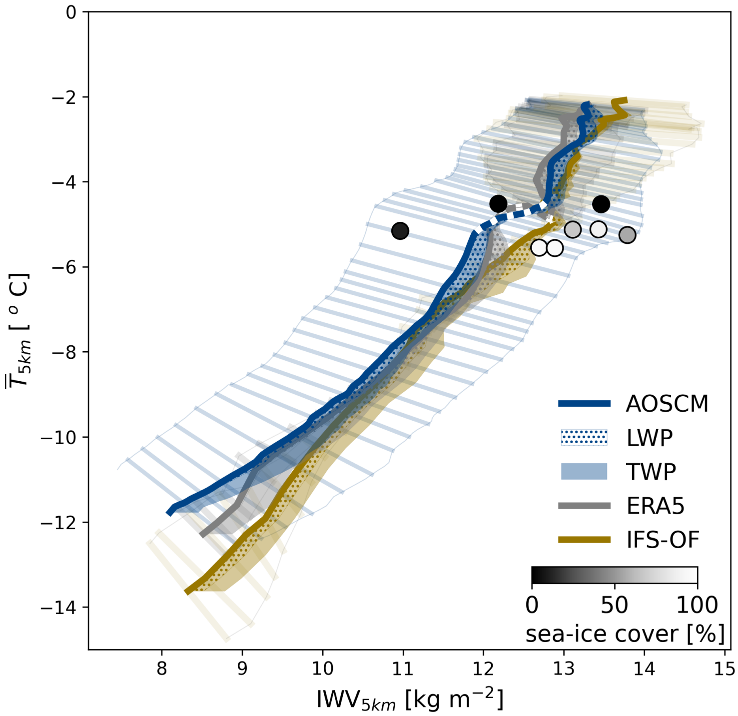


**Figure 4.** Mean airmass temperature ($\overline{T}_{5km}$, °C) and water vapor content (IWV$_{5km}$, kg m$^{-2}$) along the advection path for AOSCM simulations (blue), ERA5 (gray) and IFS-OF data (sand). The length of the faded lines crossing the mean curves shows the ensemble standard deviation while their slope shows ratio of the individual components (temperature and moisture content). Observations are shown with dots, shaded according to the sea-ice fraction of the closest ERA5 column at sampling time. Drawing the MIZ with a dashed line helps distinguish the sections of the airmass transformation taking place over different surface types.

https://doi.org/10.5194/egusphere-2024-3709
Preprint. Discussion started: 13 January 2025


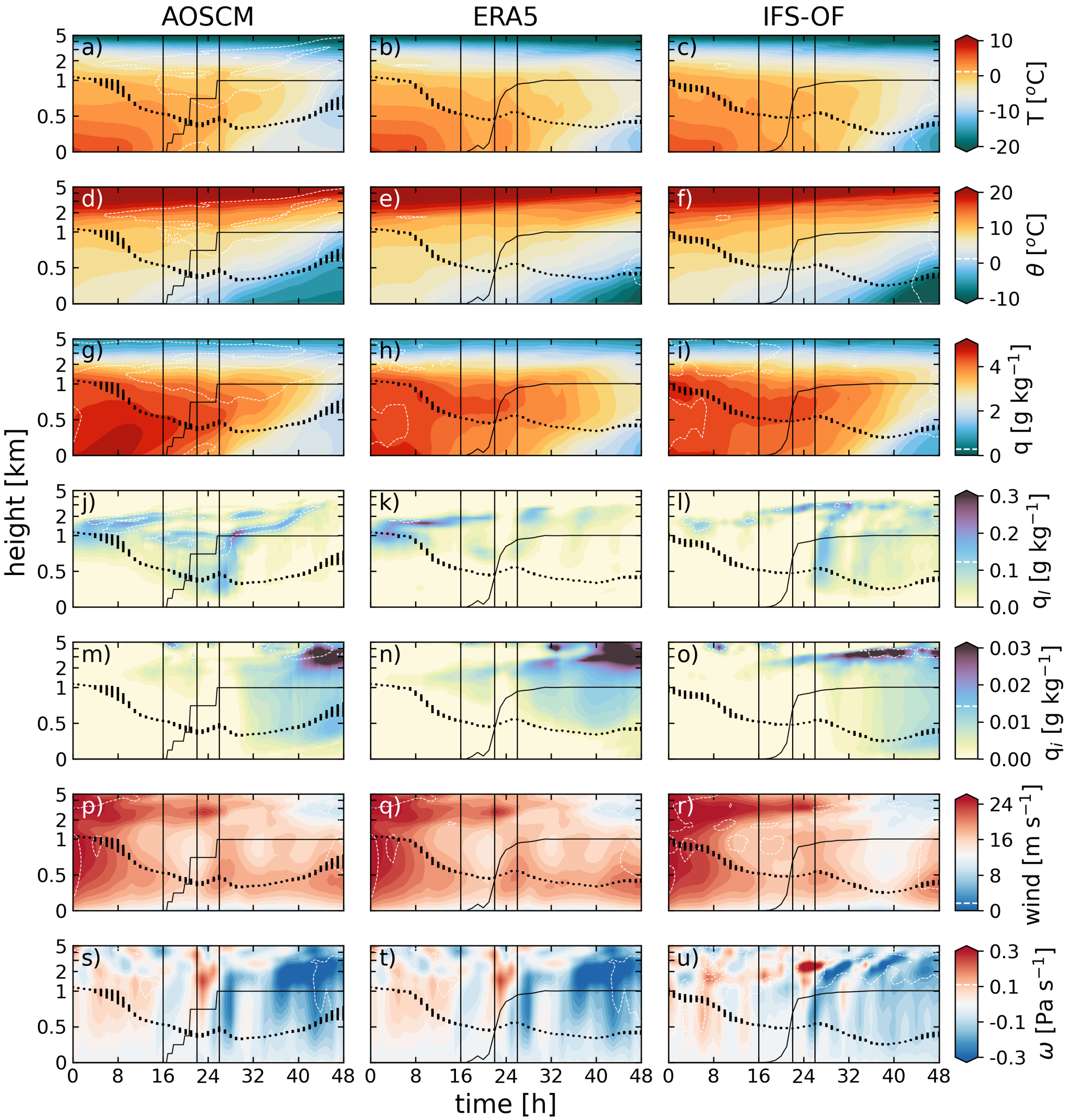


**Figure 5.** Time-height cross-sections of the ensemble average a-c) temperature, d-f) potential temperature (°C), g-i) specific humidity (g kg$^{-1}$), j-l) specific liquid and, m-o) ice water content (g kg$^{-1}$), p-r) horizontal and s-u) vertical wind speed (m s$^{-1}$) along along the trajectories in the AOSCM simulations (left column), ERA5 (middle column) and IFS-OF data (right column). The height axis is linear below 1 km and logarithmic above. The grey-scale dashed contours show the ensemble standard deviation; contour intervals are marked on the respective colorbars. The dotted line marks the ensemble mean PBL height and the sizes of the dot markers represents the ensemble deviation. The black solid line shows the along-stream sea-ice concentration.

https://doi.org/10.5194/egusphere-2024-3709
Preprint. Discussion started: 13 January 2025


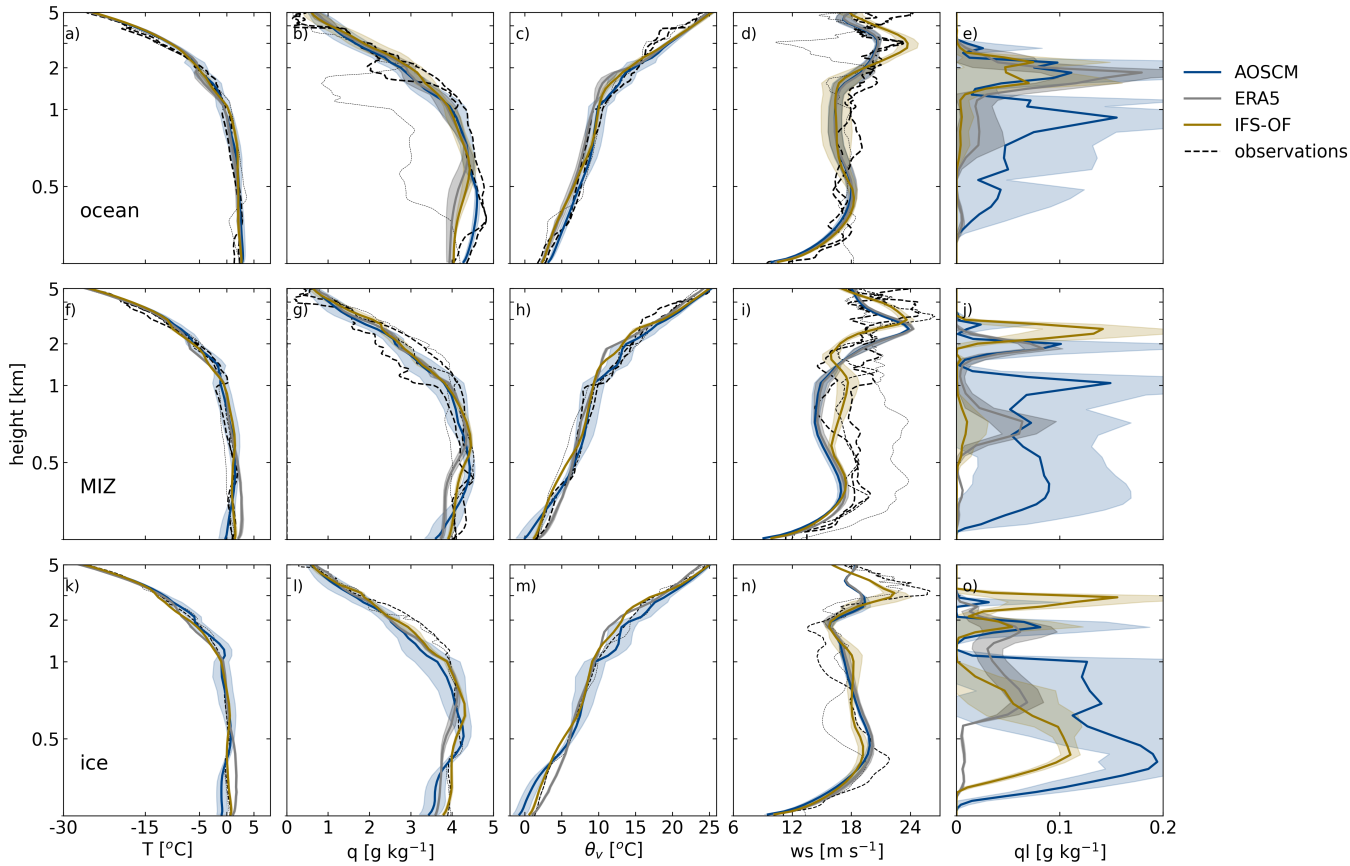


**Figure 6.** Vertical profiles of temperature (°C), specific humidity (g kg$^{-1}$), potential temperature, wind speed and specific cloud liquid water content (g kg$^{-1}$) over the ocean(a-e), MIZ(f-j) and sea-ice(k-o). Observations are shown with black dashed lines; their thickness represents their proximity to the AOSCM (blue), ERA5 (gray) and IFS-OF (gold) reference profiles for each surface type. The reference profiles were taken close to the majority of the observations (over or around the MIZ) and are denoted with black vertical lines in Fig. 5. The height axis is linear below 1 km and logarithmic above.

https://doi.org/10.5194/egusphere-2024-3709
Preprint. Discussion started: 13 January 2025


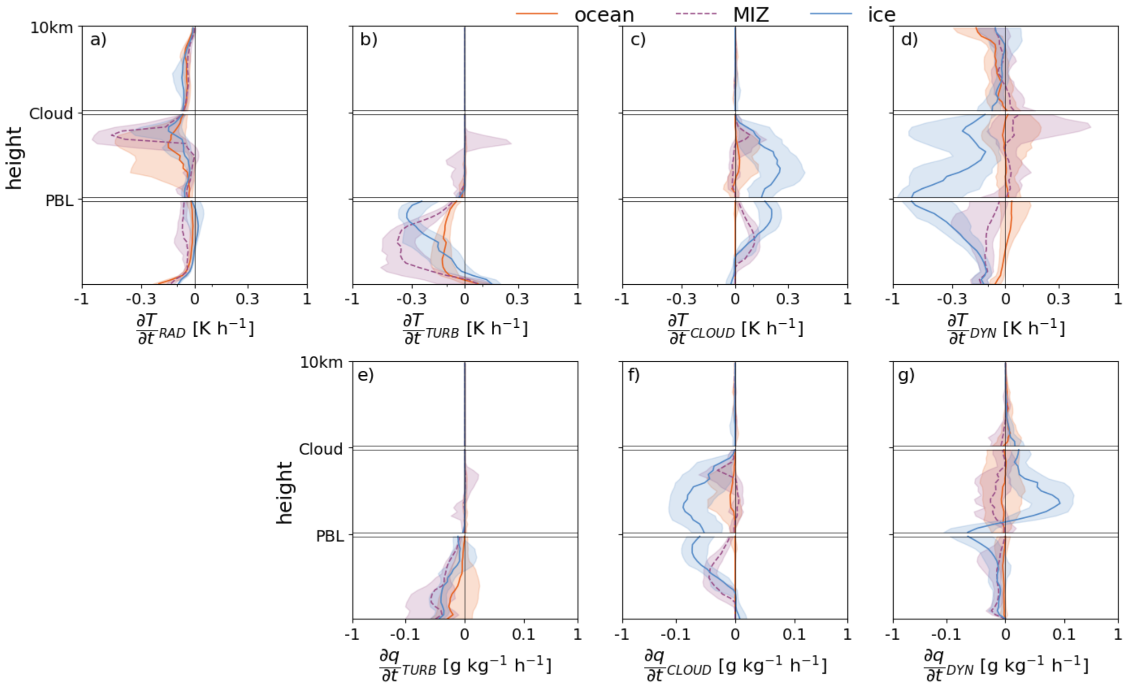


**Figure 7.** Tendencies of temperature (K h$^{-1}$) attributed to a) radiation ($\frac{\partial T}{\partial t}_{RAD}$), b) turbulence ($\frac{\partial T}{\partial t}_{TURB}$), c) cloud ($\frac{\partial T}{\partial t}_{CLOUD}$) and d) dynamical processes ($\frac{\partial T}{\partial t}_{DYN}$) over the ocean (orange), MIZ (purple) and sea-ice(blue) leg. The ensemble median tendency profiles (solid lines) and the 25th and 75th percentiles (shaded areas around solid lines) have been computed over the length of their corresponding leg of the transformation, separately for three sub-layers within the airmass (PBL, cloud and residual layer up to 10 km).